To appear in the *Journal of Geophysical Research*, 2001.

The annual cycle of water vapor on Mars as observed by the Thermal Emission Spectrometer

Michael D. Smith
NASA Goddard Space Flight Center, Greenbelt, Maryland

Abstract

Spectra taken by the Mars Global Surveyor Thermal Emission Spectrometer (TES) have been used to monitor the latitude, longitude, and seasonal dependence of water vapor for over one full Martian year (March 1999–March 2001). A maximum in water vapor abundance is observed at high latitudes during mid-summer in both hemispheres, reaching a maximum value of ~100 pr-μm in the north and ~50 pr-μm in the south. Low water vapor abundance (<5 pr-μm) is observed at middle and high latitudes in the fall and winter of both hemispheres. There are large differences in the hemispheric (north versus south) and seasonal (perihelion versus aphelion) behavior of water vapor. The latitudinal and seasonal dependence of the decay of the northern summer water vapor maximum implies cross-equatorial transport of water to the southern hemisphere, while there is little or no corresponding transport during the decay of the southern hemisphere summer maximum. The latitude-longitude dependence of annually-averaged water vapor (corrected for topography) has a significant positive correlation with albedo and significant negative correlations with thermal inertia and surface pressure. Comparison of TES results with those retrieved from the Viking Orbiter Mars Atmospheric Water Detectors (MAWD) experiments [*Jakosky and Farmer*, 1982] shows some similar features, but also many significant differences. The southern hemisphere maximum observed by TES was not observed by MAWD and the large latitudinal gradient in annually-averaged water vapor observed by MAWD does not appear in the TES results.

1. Introduction

Although water vapor is a minor constituent in the atmosphere of Mars, it still plays an important role. Along with the annual cycles of CO_2 and dust, the annual water cycle is one of the three main cycles that define the present Mars climate. Since the first detection of water vapor on Mars by *Spinrad et al.* [1963] there have been many additional observations, both from ground-based observers and from spacecraft. *Jakosky* [1985] and *Jakosky and Haberle* [1992] give good reviews of water vapor measurements.

Since the time of the Viking mission, the definitive description of the seasonal and latitudinal dependence of water vapor has been that derived from the Viking Orbiter Mars Atmospheric Water Detectors (MAWD) [*Farmer et al.*, 1977; *Jakosky and Farmer*, 1982]. That data set shows a global annual average of about 10 pr-μm of water with higher values over the northern hemisphere in the northern summer reaching a maximum of ~90 pr-μm near the north pole at about L_s = 120°. Although interannual variability has been noted [e.g. *Clancy et al.*, 1992; *Sprague et al.*, 1997], most ground-based observations of water vapor have been more-or-less consistent with the general pattern observed by MAWD. Notable exceptions to the MAWD trend were the observation by *Barker et al.* [1970] of a maximum in water vapor abundance (reaching 30–40 pr-μm) in the southern summer season compared to the very weak maximum in the MAWD data of 10–15 pr-μm at that season, and the observation by Barker of a somewhat higher water vapor column (15–20 pr-μm) at all seasons during the two Mars years 1972–1976 [*Jakosky and Barker*, 1984].

The Thermal Emission Spectrometer (TES) onboard the Mars Global Surveyor (MGS) has been in mapping orbit around Mars since March 1999, and now provides an excellent opportunity to examine the column abundance of water vapor over an entire Mars year in great detail. Previous results of atmospheric thermal structure and aerosol distribution from TES are given by *Smith et al.* [2001], *Pearl et al.* [2001], *Conrath et al.* [2000], *Smith et al.* [2000a,c] and *Christensen et al.* [1998]. In this paper we report the results of one Mars year of TES monitoring of water vapor.

In section 2 we give a brief description of the TES instrument and the data taken during the mapping orbit. More detailed information is given by *Christensen et al.* [1992; 2001]. In section 3 we describe the algorithm used for the retrieval of water vapor column abundance. In section 4 we present our results and compare them with Viking MAWD and ground-based observations. We discuss our findings in section 5, and summarize in section 6.

2. Data Set

The Mars Global Surveyor mapping orbit gives one narrow strip of observations running roughly north-south. One day of data gives two sets of twelve such strips spaced roughly 30° apart in longitude, with one set taken near a local time of 0200 and the other near 1400. For this work, we use only the nadir-geometry daytime (1400 hours) data. We do not use nighttime data because they have lower signal-to-noise and the atmospheric temperature profiles retrieved from nighttime TES data potentially have relatively large uncertainties near the surface where water vapor is often concentrated. This is because the km-scale vertical structure of the near-surface boundary layer nighttime temperature inversion observed in the MGS radio occultation profiles [*Hinson et al.*, 1999] cannot be resolved by TES.

To obtain a global- and seasonal-scale view of water vapor abundance we average the long wavelength portion of daytime nadir-geometry TES spectra into bins that are 2° wide in latitude and 2° wide in season (L_s). All longitudes are binned together, so these represent zonal averages. This results in ~11000 bins. Spectra are averaged separately for the two spectral resolutions (6.25 and 12.5 cm^{-1}) that are used by TES. The results presented below were retrieved using data starting with the beginning of the mapping portion of the MGS mission at L_s = 104° (March 1, 1999) and extending for just over one full Mars year to L_s = 137° (March 28, 2001). The TES operated nearly continually during this entire period with only minor exceptions. Several million spectra were used in this analysis.

3. Water Vapor Retrieval Algorithm

Figure 1 shows a line-by-line synthetic water vapor spectrum convolved to the TES resolution of 6.25 cm^{-1}. At this spectral resolution, TES has a sampling interval of about 5.3 cm^{-1}. To retrieve water vapor abundance, we use the rotation bands in the region 240–360 cm^{-1} (28–42 μm). At 6.25 cm^{-1} resolution the hundreds of individual water vapor lines that lie in this spectral region are combined into five main bands spaced roughly 20–30 cm^{-1} apart. This spec-

tral region is a favorable place to perform a retrieval because at these wavelengths the TES signal-to-noise is relatively high (~500), the opacity from dust and water-ice is relatively low [*Smith et al.* 2000a,b], and the distinctive, "picket-fence" spectral dependence of the water vapor bands allows the contribution from water vapor to the spectrum to be easily separated from the contributions from dust, water ice, and the surface.

The TES contains a 2x3 array of detectors. Because optical path lengths in the instrument are slightly different for each detector, the wavenumbers sampled by each detector for a given TES sample number are slightly offset (by as much as a couple of cm^{-1}). Water vapor rotation bands have sufficient spectral structure (see Fig. 1) that spectra from different detectors cannot be averaged together without significantly "smearing out" the bands. Therefore, we only use spectra from TES detector 2, which has the advantage of being one of the two detectors nearest the central ray of the instrument. We have calibrated the wavenumber scale by shifting the grid of wavenumbers as a function of TES sample number until the shape and amplitude of water vapor lines observed in the TES spectra best match the synthetic spectrum. This wavenumber calibration is quite sensitive. A variation of one-tenth of the TES sampling (or about 0.5 cm^{-1}) results in a noticeably worse fit. The resulting sampling of the water vapor spectrum is shown as points on the synthetic spectrum in Fig. 1.

3.1. Model Atmosphere

For each L_s/latitude bin, the thermal structure of the atmosphere is taken to be the average of all atmospheric temperature profiles available for that bin. Atmospheric temperatures are retrieved from each TES observation (each footprint of 2x3 detectors) as part of the standard operational TES processing using a constrained linear inversion of observed radiance in the 15-μm CO_2 band [*Conrath et al.* 2000]. The surface temperature for each bin is taken to be the average brightness temperature in the relatively transparent spectral window between 1285 and 1315 cm^{-1} for all available spectra in that bin.

Water vapor absorption is computed using the correlated-k method [for example, *Goody et al.*, 1989]. Correlated-k coefficients for an array of different temperatures and pressures are computed using a line-by-line computation of water vapor transmittance. Water vapor line parameters are obtained from the GEISA-97 database [*Husson et al.* 1992]. For the water vapor lines of interest, the line parameters from GEISA-97 are essentially identical to those of the HITRAN-2000 database. An approximate correction is made to the line widths to account for CO_2-broadening of water vapor (see section 3.5). The vertical distribution of water vapor is approximated as being well-mixed with the CO_2 gas up to the water vapor condensation level and then zero above that. The condensation level is a function of both the atmospheric temperature profile and the water vapor column abundance. Therefore, an initial guess for the water vapor column abundance is used to compute an initial condensation level and then the entire retrieval is iterated until a self-consistent solution is obtained. Typically no more than two or three iterations are required for convergence.

3.2. Equivalent opacity and band depth index

The first step in the water vapor retrieval algorithm is to convert the averaged observed radiance spectrum, $I_{\rm obs}(\nu)$, in each L_s/latitude bin to an equivalent opacity spectrum, $\tau_0(\nu)$, through numerical solution of the radiative transfer equation:

$$I_{\rm obs}(\nu) = \epsilon(\nu) B[T_{\rm surf}, \nu]\, e^{-\tau_0(\nu)/\mu} + \int_0^{\tau_0(\nu)} B[T(\tau), \nu]\, e^{-\tau/\mu}\, d\tau, \qquad (1)$$

where ν is frequency, μ is the cosine of the emission angle, $B[T, \nu]$ is the Planck function, $T_{\rm surf}$ is the surface temperature, $T(\tau)$ is the atmospheric temperature, and the integral is performed from the spacecraft (at $\tau = 0$) to the surface (at $\tau = \tau_0$).

The above equation neglects scattering and the solar beam, and assumes a plane-parallel geometry. These are excellent approximations for the observation of water vapor in the TES nadir-geometry mode at 240–360 cm^{-1}. The integral in opacity is evaluated by assuming that the opacity source is well-mixed up to the water vapor condensation level and then zero above that.

The opacity spectrum obtained from solution of (1) contains opacity from water vapor, dust aerosol, water ice aerosol, and the effect of a non-unit surface emissivity. The contribution from water vapor is estimated by removing a continuum opacity from each of the five main water vapor bands. The underlying assumption is that the spectral signatures of dust, water ice, and surface emissivity are approximately linear over the narrow spectral range (about

20 cm^{-1}) of each individual water vapor band [*Smith et al.* 2000a,b; *Bandfield et al.* 2000a]. An overall water vapor band depth index for the 6.25 cm^{-1} resolution data, $\tau_{6.25}$, is then formed by averaging the continuum-removed opacities for the five bands as follows:

$$\tau_{6.25} = \Big[-\tau_0(18)+\frac{2}{3}\Big[\tau_0(19)+\tau_0(20)+\tau_0(21)\Big]-\tau_0(22)-$$
$$\tau_0(24) + 2\tau_0(26) - \tau_0(28) - \tau_0(29)+$$
$$2\tau_0(30) - \tau_0(31) - \tau_0(33) + 2\tau_0(35)-$$
$$\tau_0(37) - \tau_0(38) + 2\tau_0(40) - \tau_0(42)\Big]/12, \quad (2)$$

where the numbers in parentheses indicate the TES sample number (see Fig. 1). Similarly, an overall water vapor band depth index can be formed for the 12.5 cm^{-1} resolution data, $\tau_{12.5}$, by averaging the continuum-removed opacity for the bands observed in 12.5 cm^{-1} data.

3.3. Cross-calibration of 6.25 and 12.5 cm^{-1} data

Most of the spectra taken by TES before $\sim L_s$ = 90° (December 2000) were taken in the 12.5 cm^{-1} spectral resolution mode, while most of the spectra taken after L_s = 90° were taken in the 6.25 cm^{-1} spectral resolution mode. Figure 2 shows a comparison of TES observations of water vapor at 6.25 cm^{-1} and 12.5 cm^{-1} taken at nearly the same time (L_s = 307°) and location (79°S latitude). Although it is possible to perform the water vapor retrieval separately for each spectral resolution, we have found it more convenient to convert the strength of the water vapor bands observed in the 12.5 cm^{-1} mode to an equivalent strength as observed in the 6.25 cm^{-1} mode, and then to perform a single retrieval using the equivalent 6.25 cm^{-1} value of the water vapor band depth index. We have chosen to convert to 6.25 cm^{-1} resolution because the water vapor bands are much more clearly defined at 6.25 cm^{-1} than they are at 12.5 cm^{-1} and so a more accurate retrieval can be performed.

Most of the L_s/latitude bins contain only one spectral resolution or the other, but there are still over 1800 bins that contain at least 10 spectra from each resolution. These bins are used to find how the observed water vapor band depth at 12.5 cm^{-1} relates to that observed at 6.25 cm^{-1}. Figure 3 shows the relation between the 6.25 and 12.5 cm^{-1} water vapor band depth indices. The data are well-described by the empirical linear relation

$$\tau_{6.25} = 1.45\ (\tau_{12.5} - 0.0035). \quad (3)$$

For each L_s/latitude bin, the 6.25 and 12.5 cm^{-1} water vapor band depth indices are computed, and the band depth for the 12.5 cm^{-1} resolution data is converted to an equivalent 6.25 cm^{-1} resolution value using (3). The final band depth index for each bin is then given by the average of the band depth index from the 6.25 cm^{-1} data and the equivalent band depth index inferred from the 12.5 cm^{-1} weighted by the number of spectra at each resolution.

3.4. Water vapor column abundance from band depth index

The conversion from a water vapor band depth index to a column abundance is performed for each L_s/latitude bin by computing a suite of synthetic water vapor spectra at a range of different column abundances. The synthetic spectra are computed at 6.25 cm^{-1} spectral resolution and at the wavenumbers sampled by TES. The synthetic spectrum is converted first to opacity spectra using (1) and then next to water vapor band depth index using (2). Water vapor column abundance is solved numerically by variation of the column abundance until the band depth index from the synthetic data matches the observed band depth. At this point a new water vapor condensation level is computed using the new estimate of water vapor column abundance and the entire retrieval process is iterated until convergence is obtained.

Figure 4 shows the resulting fit for one L_s/latitude bin (centered at 43° N latitude, L_s = 85°) shown in terms of opacity. A continuum has been removed from the TES opacity spectrum. The fit is excellent over the five bands that are used in the retrieval (between 240 and 360 cm^{-1}) and still remains good for the strong band centered at 225 cm^{-1} and the weaker bands at 370–400 cm^{-1} which are not used in the retrieval. Both the relative amplitudes and spectral dependence (or shape) of the bands are well-reproduced. The retrieved water vapor column abundance for this case is 25 pr-μm.

3.5. Water Vapor Line Broadening by Carbon Dioxide

Synthetic water vapor spectra are computed using the correlated-k formulation. The correlated-k coefficients are derived from a very high resolution

line-by-line computation of the water vapor spectrum using water vapor line strengths and widths from the GEISA-97 database. However, the line widths given in the GEISA-97 database are for water vapor broadened by terrestrial air, not by CO_2 as appropriate for Mars. For water vapor abundances and atmospheric pressures typical for Mars, the net result at TES spectral resolution of an increase in line width is a decrease in water vapor transmittance (or an increase in water vapor opacity). It is important to carefully consider the effect of CO_2 broadening and to make this correction to the line widths because the effect on the retrieved water vapor column abundance is substantial. The value for CO_2 broadening chosen below for this retrieval results in a reduction of ~40% in water vapor abundance.

We will call the ratio of the CO_2-broadening coefficient for water vapor to the air-broadening coefficient for water vapor, the "broadening ratio". A value of the broadening ratio greater than unity indicates that water vapor lines are broader in a certain partial pressure of CO_2 than they are in the same partial pressure of air (as given by the GEISA-97 database). There is little experimental data on the broadening ratio. Laboratory measurements of CO_2 broadening in the near-infrared by *Gamache et al.* [1995] indicate a broadening ratio between about 0.9 and 1.8 depending on the particular transition. However, none of the lines for which line widths measured were in the wavenumber range used in this retrieval. In modeling Venus near-infrared spectra, *Pollack et al.* [1993] and *Crisp et al.* [1991] have estimated CO_2 broadening of water vapor by using a constant broadening ratio of 1.3 based on work by *Howard et al.* [1956]. In modeling Mars microwave spectra, *Clancy et al.* [1992] have used a constant broadening ratio of 1.6 based on work by *Liebe and Dillon* [1969]. None of these estimates for the broadening ratio is for the water vapor lines used in our retrieval. Given this lack of information and consensus, we choose to adopt a constant value for the broadening ratio of 1.5 that is roughly consistent with all of the above. We note (as elaborated below in section 3.6) that uncertainty in this parameter leads to an uncertainty in the overall scaling of our water vapor column abundance estimates.

3.6. Estimation of Uncertainties

The algorithm used to retrieve water vapor column abundance has a number of steps, and there are at least seven main sources for uncertainty in the final retrieved value: 1) instrument noise and calibration, 2) the retrieval of surface and atmospheric temperatures, 3) the assumed vertical distributions of dust and water vapor, 4) the removal of a continuum opacity from sources other than water vapor, 5) the cross-calibration of 6.25 and 12.5 cm^{-1} resolution data, 6) the calculation of synthetic water vapor opacity, and 7) the estimation of the effect of CO_2 broadening on water vapor.

The uncertainty introduced by instrument noise and calibration is relatively small. For daytime conditions, the typical instrument noise of 3×10^{-8} W cm^{-2} sr^{-1} / cm^{-1} [*Christensen et al.*, 1992, 1998, 2001; Christensen, 1999] gives an opacity error of about 0.02 for any one particular TES spectral sample. However, since we use 17 TES spectral samples (in the 6.25 cm^{-1} mode) the error in the observed band depth index is much smaller. The absolute TES calibration is quite good, and errors that do occur tend to have little spectral structure (for example, a nearly constant offset). This type of error is effectively removed when we compute the band depth index and subtract the continuum opacity. Uncertainties contributed by the retrieved surface and atmospheric temperatures can be of order 0.03 for a particular TES spectral sample [*Smith et al.*, 2000a], but this is a systematic error that tends to be nearly an offset in the opacity and is therefore removed in the continuum when the band depth index is computed.

There is not sufficient information in a TES nadir-geometry spectrum to retrieve the vertical distribution of dust or water vapor independently. TES limb-geometry spectra can potentially provide information on the vertical profile of dust and water vapor above a height of 10 km [*Smith et al.*, 2000c], but that retrieval is not yet operational, and is beyond the scope of this work. We have taken the vertical distribution of dust to be well-mixed, which has been found to be a good approximation for dust in Viking [*Pollack et al.*, 1977], Pathfinder [*Smith et al.*, 1997] and TES data [*Smith et al.*, 2000a]. We have taken the water vapor vertical dependence to be that of a well-mixed profile below the water condensation level and zero above it. Analysis of the vertical distribution of water vapor by *Rodin et al.* [1997], *Burgdorf et al.* [2000], and *Gurwell et al.* [2000] are all consistent with this assumption. The water vapor profile could be made to follow the saturation condensation curve above the condensation level, but that value drops off very quickly with height and its contribution to the total column abundance is negligible. For the dust loadings observed by TES during the period consid-

ered here, we estimate the uncertainty introduced by the assumed vertical distributions of dust and water vapor to be ~5% or less.

The computation of a water vapor band depth index by removal of a continuum opacity level contains the implicit assumption that the spectral dependence of the contribution to the effective opacity from all other sources (dust and water ice aerosols and a non-unit surface emissivity) varies smoothly over the spectral width of one water vapor band (20–30 cm^{-1}) in the spectral range considered (240–360 cm^{-1}). The spectral dependence of dust and water ice aerosol do indeed have much less spectral structure on that scale than does water vapor [*Smith et al.*, 2000a,b; *Bandfield et al.*, 2000a]. On a global scale, the two major surface emissivity spectral shapes (a basaltic and a basaltic-andesite composition) also have much less spectral structure in this spectral region than water vapor [*Bandfield et al.*, 2000b]. Hematite has some significant spectral structure at the frequencies of interest, but it is at the 50–100 cm^{-1} scale [*Christensen et al.*, 2000]. Hematite features are observed over only a very limited portion of the surface and we expect the features to be mostly removed by the continuum removal process. Therefore, the total uncertainty in the water vapor band depth index caused by the continuum removal is small.

The above four sources of uncertainty occur in the process of finding the water vapor band depth index. All four are relatively small and we estimate that the total uncertainty in the index for 6.25 cm^{-1} resolution data to be no more than 0.003 (with typical values of the index ranging from 0.03 to 0.10, see Fig. 3). The uncertainty in the index for 12.5 cm^{-1} resolution data may be somewhat higher because of the fewer number of points used in forming the index. The largest uncertainty in obtaining a final averaged band depth index for a particular L_s/latitude bin is likely caused by uncertainty in the calibration of 12.5 cm^{-1} resolution index values relative to those at 6.25 cm^{-1}. Figure 3 shows the relation between the two, and the spread of points around the given linear relation gives an indication of the uncertainty which appears to be roughly 0.005–0.010 (i.e. ~10–20%) in a root-mean-square sense.

The final two sources of uncertainty come from the process of calibrating the water vapor band depth index to a column abundance in precipitable microns. The computation of a water vapor band depth index based on a synthetic water vapor spectrum involves a different set of uncertainties than that described above for computation of the observed band depth. There is no longer a contribution from instrument noise and calibration or from removal of a continuum opacity from other sources. However, there are new uncertainties not present when using the observed data, such as uncertainty in the H_2O line strengths, positions, and shapes (line widths will be discussed separately, below) and error caused by use of the correlated-k approximation. The first three uncertainties are very difficult to estimate, but based on the excellent fits we get to the observed data (see Fig. 4), we believe this is not a dominant source of uncertainty. Results from the correlated-k method can be directly compared with "exact" line-by-line calculations to evaluate the error involved with using the correlated-k approximation. With the 20 correlated-k integration points that we use, errors are typically $\leq$1–2%.

The largest source of uncertainty in the end-to-end retrieval algorithm is in our assumption of a value for the broadening ratio, defined above as the amount of water vapor line-broadening by CO_2 compared to that by terrestrial air (as tabulated in the GEISA and HITRAN databases). This uncertainty enters as a systematic error essentially multiplying all results by a nearly-constant factor. The value of 1.5 assumed here leads to an increase in the water vapor band depth index of about 20% over that for terrestrial air-broadening. The individual water vapor lines being observed are highly saturated and are therefore in the regime where opacity goes as the square-root of abundance. Thus, abundance goes as opacity (or the band depth index which is based on opacity) squared and our nominal value for the broadening ratio gives an abundance ~40% lower than would be obtained with terrestrial air-broadening. The likely value for the true broadening ratio (averaged over the important lines) is between 1.2 and 1.8 (see Section 3.5) meaning that there could be an error in retrieved water vapor column abundance of order ±25%. Note that this error would affect all retrieved water vapor amounts by a similar factor and would have very little effect on the dependence of water vapor as a function of L_s and latitude.

In summary, the largest source of random error is the cross-calibration of 6.25 and 12.5 cm^{-1} data. The total estimated random error is 0.005–0.010, which corresponds to an uncertainty in water vapor column abundance of about 3–5 pr-μm. A significant systematic error of as much as 25% is possible through uncertainty in the broadening ratio. This would re-

sult in a nearly-constant multiplicative factor being applied to all water vapor column abundances and would not affect the distribution of water vapor as a function of season and latitude.

4. Results

The top panel of Plate 1 shows the column abundance of water vapor observed by TES as a function of season (L_s) and latitude. Water vapor abundance is shown for the MGS mapping period between L_s = 104°, March 1, 1999 and L_s = 137°, March 28, 2001. Results include only daytime data (local time ~1400) where the surface temperature is >220 K. Results have been zonally averaged into bins that are 2° wide in latitude and 2° wide in L_s. The total integrated water column integrated perpendicularly from the surface to infinity is shown. No attempt has been made here to correct for topography or to scale to an equivalent pressure surface.

4.1. Overview

The TES water vapor results (top panel of Plate 1) show a strong maximum in the northern hemisphere summer. A peak water column of ~100 pr-μm was attained in each of the two Martian years observed poleward of 80°N latitude at L_s = 110°–120°. At L_s = 120°, water vapor abundance dropped off monotonically from north to south with an abundance of 50 pr-μm at 60°N latitude, 20 pr-μm at 15°N latitude, and less than 5 pr-μm of water vapor south of 20°S latitude. After L_s = 130°, water vapor abundance declined rapidly at high northerly latitudes falling below 10 pr-μm by L_s = 170°. However, the water vapor abundance at low northerly latitudes continued to increase during this time forming a tongue of high water vapor abundance extending equatorward and to later season from middle northerly latitudes. For any particular latitude in the northern hemisphere, the peak water vapor column abundance occurred progressively later in the season for lower northern latitudes. At 80°N latitude, water vapor column abundance reached a maximum value at L_s = 115°, as compared to L_s = 135° for 45°N latitude and L_s = 150° for 30°N latitude. The equatorial water vapor column exhibited a broad maximum between L_s = 180° and 210°. By L_s = 170° a well-developed maximum in water vapor appeared between the equator and 30°N latitude. This maximum in water vapor as a function of latitude at 0°–30°N latitudes persisted throughout northern fall and winter until L_s = 40° in the following year, when water vapor abundance rapidly increased throughout the northern hemisphere.

In the southern hemisphere there was a gradual rise in water vapor abundance throughout southern winter and spring as water vapor appeared to be transported southward from the northern hemisphere. In late southern spring (L_s = 220°), water vapor at low southerly latitudes decreased somewhat, while water vapor at middle and high southerly latitudes increased. A maximum in southern hemisphere water vapor was reached at L_s = 290° with a column abundance of ~40 pr-μm poleward of 75°S latitude. At this time there was a local minimum in the latitudinal dependence of water vapor at 10°–30°S latitude and a small local maximum at 0° and 30°N latitude, which may be caused by transport of water vapor from the southern hemisphere to the north via the Hadley circulation. The latitudinal dependence of water vapor in the southern summer at L_s = 290° was very different than that in the northern summer at L_s = 110°. While there was significant water vapor at high latitudes near the summer pole in both seasons, the northern hemisphere summer maximum was stronger and did not show a secondary low-latitude maximum in the winter hemisphere.

Water vapor abundance decreased from the southern summer polar maximum after L_s = 300°, and decreased planetwide after L_s = 330°. The period between L_s = 330° and 40° exhibited minimum water vapor abundance with the average global abundance of 7–8 pr-μm. Water vapor abundance began to increase significantly in the northern hemisphere after L_s = 40°, steadily climbing to its peak value L_s = 120° while the southern hemisphere water vapor remained relatively unchanged at a very low level.

4.2. Comparison with Viking MAWD

The bottom panel of Plate 1 shows water vapor column abundance retrieved from the Viking Orbiter Mars Atmospheric Water Detectors (MAWD) [*Farmer et al.*, 1977; *Jakosky and Farmer*, 1982]. There are some broad similarities between the MAWD and TES results. The most obvious similarity is the magnitude and timing of the north polar summertime maximum in water vapor abundance. Both MAWD and TES show >75 pr-μm water vapor poleward of 75°N latitude from L_s = 100°–125°. In fact, the general dependence of water vapor on L_s and latitude between about L_s = 75° and 140° is fairly similar, although TES water vapor abundance is somewhat

higher at low latitudes. Both data sets also indicate that the timing of the northern hemisphere maximum occurs later in season with decreasing latitude. Another similarity between the MAWD and TES results is the existence of a generally low amount of water vapor in middle and high latitudes in the winter hemisphere (in both the north and the south).

Although the above features of the MAWD and TES water vapor L_s/latitude maps are similar, there are also a number of very significant differences. Figure 5 shows the ratio of TES to MAWD water vapor abundance as a function of L_s and season. The largest distinction arises from the appearance of a strong maximum in water vapor at south polar latitudes just after summer solstice in the TES results. No such maximum appears in the MAWD results. Interannual variability likely accounts for some of this difference, but some of the difference is associated with an observational bias in the MAWD data caused by two global, or "planet-encircling" dust storms which began near L_s = 205° and 274°. As indicated in the MAWD papers [*Farmer et al.*, 1977; *Davies*, 1979; *Jakosky and Farmer*, 1982], scattering of the solar radiation by dust and water ice biases the MAWD water vapor abundance to lower values because the observed radiation does not sample the entire column of water vapor. *Davies* [1979] estimated that a visible dust opacity of 0.5 would result in a derived water vapor abundance 10% lower than actual. *Jakosky and Farmer* [1982] estimated that a visible dust opacity of 1.0 would result in a derived water vapor abundance 20% lower than actual, and they suggested that the MAWD water vapor abundance should be considered as a lower limit when visible opacity is greater than unity.

During the first Viking year (1977), there were two planet-encircling dust storms. Drops in MAWD water vapor at all latitudes are apparent in Plate 1 at both L_s = 205° and 270°, with the low values persisting beyond L_s = 330°. Visible aerosol opacity measured by the two Viking Landers [*Colburn et al.* 1989] indicates that opacities greater than unity existed during the entire period between L_s = 205° and 330° for both landers. The shading in Fig. 5 shows L_s/latitude bins where the infrared dust opacity inferred from the Viking Orbiter Infrared Thermal Mapper (IRTM) instrument [*Martin*, 1986; *Martin and Richardson*, 1993] is >0.4 (equivalent to visible opacity >∼0.8). The IRTM dust opacities are >0.4 for the period L_s = 205°–330° over much of the planet, in good qualitative agreement with the corresponding visible dust opacities of *Colburn et al.* [1989]. The solid line bounding the contours on the top and bottom in Fig. 5 represents the latitude limit for which both TES and MAWD data exist (IRTM dust opacity coverage is comparable). As further indication of the large influence of dust on MAWD results, the one area of clearing between the two planet-encircling dust storms at L_s = 250°–270°, 30°–60°S latitude corresponds closely with a noticeable increase in MAWD water vapor abundance (see Plate 1). Nevertheless, it is interesting to note that although the MAWD results are clearly biased by dust scattering, real interannual variability may contribute to the differences between TES and MAWD results. The Viking IRTM did not observe significantly elevated dust opacity at the highest southerly latitudes during the second planet-encircling dust storm (L_s = 280°–310°, 70°–85°S latitude) [*Martin and Richardson*, 1993] as seen in Fig. 5. Dust opacities there were comparable to those in the relatively clear period between the two dust storms mentioned above (L_s = 250°–270°, 30°–60°S latitude). The lack of any increase in MAWD water vapor in the region L_s = 280°–310°, 70°–85°S latitude despite the high water vapor observed then by TES suggests that the southern hemisphere water vapor maximum may have been significantly reduced in 1977.

We conclude that for the dusty period between L_s = 205° and 330°, 1) the MAWD water vapor results are biased low by a as much as a factor of 3 and should be regarded as a lower limit of actual water vapor abundance, and 2) the L_s and latitude dependence of the MAWD water vapor results is not accurate. This is consistent with the recommendations made in *Jakosky and Farmer* [1982]. The water vapor abundance retrieved from TES spectra are only very minimally affected by dust because dust scattering is much less important at TES wavelengths (∼30 μm) than at the MAWD wavelength (1.38 μm). Furthermore, dust loading levels during the TES operations (1999–2001) [*Smith et al.*, 2001] were much smaller than those present during the 1977 period of MAWD observations.

Outside of the dusty period L_s = 205°–330° there remain small, but significant differences between the MAWD and TES water vapor maps. Most apparent is at low northerly latitudes (0°–30°N) between L_s = 150° and 205° where the water vapor abundance derived from TES data is roughly 20–40% higher than that derived from MAWD data. There is also a more pronounced latitudinal gradient between L_s =

0° and 60° in the TES results, with higher water vapor abundance at 0°–30°N latitude and lower water vapor abundance at middle southerly latitudes than observed by MAWD. The increase in water vapor between L_s = 40° and 90° at 30°–70°N latitude is a gradual process in the TES results, while the MAWD results show little water vapor increase at these latitudes until an abrupt increase between L_s = 60° and 75°. These differences are likely caused by interannual variability.

Figure 5 shows that outside of the dusty L_s = 205°–330° period, the globally-averaged amount of water vapor is generally about 10–20% higher for TES than for MAWD. This may be an indication of interannual variability, but the difference is also well within the combined systematic (overall scaling) error bars for the TES and MAWD water vapor results. In the periods immediately preceding and following the two planet-encircling dust storms (L_s = 180°–205° and L_s = 330°–360°), the TES results are systematically higher by 30–75%. This could be caused by interannual variability, by a small bias in the MAWD results during these moderately dusty times, or by a combination of both.

4.3. Comparison with Ground-Based and Other Observations

In addition to the Viking MAWD data, there exists a large body of ground-based and space-based observations of Mars water vapor made at wavelengths from the visible to microwave. The three main ground-based programs that have monitored Martian water vapor extensively over the years are the ~8200-Å observations taken at McDonald Observatory [*Barker*, 1970; *Jakosky and Barker*, 1984] and by a group at the University of Arizona [*Rizk et al.*, 1991; *Sprague et al.*, 1996; 2001], and the cm and mm-wave observations taken by *Clancy et al.* [1992; 1996]. More recently, a series of observations has been taken at the Infrared Telescope Facility (IRTF) by *Novak et al.* [2001]. Space-based observations of Martian water vapor have been performed at thermal infrared wavelengths (including some of the same lines used by TES) by the Infrared Space Observatory (ISO) spacecraft [*Bergdorf et al.*, 2000] and at submillimeter wavelengths by the Submillimeter Wave Astronomy Satellite (SWAS) [*Gurwell et al.*, 2000]. Additional data sources for water vapor from Mars orbit include thermal infrared measurements from the IRIS instrument on Mariner 9 [*Hanel et al.*, 1972], from the Phobos mission using solar occultations made by the Auguste experiment [*Rodin et al.*, 1997], from the Phobos infrared-imaging spectrometer (ISM) [*Rosenqvist et al.*, 1992], and from the Pathfinder imaging system (IMP) [*Titov et al.*, 1999].

Comparison of TES water vapor abundance with the above observations is difficult given the large differences in retrieval technique, spatial resolution, temporal sampling, and local time of day. However, some general trends do emerge when the data are taken as a whole. Near L_s = 120°, nearly all observations consistently show a large peak in water vapor abundance at high northerly latitudes with lower amounts of water at low latitudes and very little water in the southern hemisphere. This general behavior is consistent with TES and MAWD results. The L_s range of 340°–90° (northern spring) seems to be a period with a relatively large amount of interannual variability. Results of *Rizk et al.* [1991], *Clancy et al.* [1992], and *Sprague et al.* [1996] vary by as much as a factor of three during this period. TES water vapor abundance tends to fall near the upper limit of this range of variation for the northern hemisphere, and near the middle or lower limit for the southern hemisphere. Near-infrared ground-based data from the IRTF taken by *Novak et al.* [2001] at L_s = 67° (January 1997) is consistent with TES data taken two Mars years later southward of 30°N latitude, but is significantly lower at middle and high northerly latitudes. Data from the Phobos/ISM instrument [*Rosenqvist et al.*, 1992] taken during this season (9 pr-μm for 0°–20°S latitude, and ~12 pr-μm for 0°–20°N latitude at L_s = 2°–18°) are in good agreement with TES data.

At L_s = 150°–160°, both the Pathfinder [*Titov et al.*, 1999] and the SWAS [*Gurwell et al.*, 2000] find very low water vapor abundances of 6 and 8 pr-μm, respectively. TES observed 24 pr-μm water vapor at the time and latitude of the Pathfinder observation (L_s = 150°, 19°N latitude), and a disk-integrated value of about 20 pr-μm at the time of the SWAS observation (L_s = 160°). It is not clear why these two observations are so low compared to TES (and to MAWD).

There are relatively few additional observations that can be used to determine the degree to which the southern summer maximum observed by TES at L_s = 260°–320° repeats each Martian year. *Barker* [1970] and *Jakosky and Barker* [1984] present disk-integrated water vapor from McDonald Observatory taken during this season. Following *Jakosky and Barker* [1984], we estimate a disk-integrated TES

value of 18 pr-μm water vapor at L_s = 220° increasing to 23 pr-μm at L_s = 280°–300° and falling to 16 pr-μm by L_s = 330°. The McDonald Observatory data from 1969, often cited as an unusually wet year are roughly consistent with the TES values through L_s = 300°. However, the very high values of 30–45 pr-μm observed at L_s = 320°–350° are at least twice as high as those observed by TES at that season. The extensive McDonald Observatory measurements made during 1972–1973 are consistently somewhat higher than MAWD, but agree better with the TES data, especially for L_s = 150°–300°. *Hanel et al.* [1972] report 10–20 pr-μm water vapor from Mariner 9 IRIS spectra at L_s = 297° and 321° in the region around the south polar cap, and observations by *Rizk et al.* [1992] made in December 1988 at L_s = 320° show a water vapor abundance of 15–20 pr-μm at high southerly latitudes. These values are lower than those observed by TES (30–40 pr-μm at L_s = 297°and 20–25 pr-μm at L_s = 320°), but substantially higher than the 5 pr-μm observed by MAWD.

The best ground-based measurements for comparison are those taken since March 1, 1999 so that a direct comparison can be made with the TES water vapor retrievals. We know of three groups that have observations of Martian water vapor during this time. The program at McDonald Observatory to monitor Mars water vapor led by E. Barker has observations from 1999 and 2000 [personal communication, 2001] but these data have not yet been reduced and calibrated. *Sprague et al.* [2001] report on observations taken at 70°–80°N latitude between at L_s = 105°–115° and at 150° in 1999 which can be directly compared with TES observations taken from the beginning of mapping. TES water vapor abundance at 70°–80°N latitude and L_s = 105°–115° cover the range ~50–100 pr-μm and so are roughly consistent, though perhaps somewhat higher than the 43–76 pr-μm reported by *Sprague et al.* [2001]. At 70°–80°N latitude and L_s = 150°, TES observations give 20–30 pr-μm water vapor which is significantly higher than the 9–17 pr-μm reported by *Sprague et al.* [2001]. Preliminary results are available from recent observations by R. Novak, M. Mumma, and M. DiSanti [personal communication, 2001] taken in the near-infrared (3.6 μm) at the IRTF on March 22, 1999 (L_s = 113°) and January 16, 2001 (L_s = 104°). The IRTF water vapor results are comparable to those of TES from the same date and latitude near the equator, but are significantly lower (by a factor of 2 or 3) than TES at middle and high northerly latitudes. This is the season where TES (and others) have consistently observed the northern hemisphere summertime maximum of water vapor.

5. Discussion

5.1. Condensation Level

An important quantity that comes out of the retrieval process is the water condensation level. The condensation level is computed in the retrieval algorithm to set the vertical distribution of water vapor. Figure 6 shows the water condensation level in terms of kilometers above the surface as a function of L_s and latitude. The condensation level is a function of atmospheric temperature and water vapor abundance, but the dependence on temperature is the dominant controlling factor. The latitude and seasonal dependence in Fig. 6 largely follows that of averaged atmospheric temperatures [compare with the top panel of Plate 1 of *Smith et al.*, 2001]. Between L_s = 0° and 180° the atmosphere is relatively cool and the condensation height is low (10–20 km above the surface). As atmospheric temperatures increase toward perihelion (currently at L_s = 251°) due to enhanced solar flux and dust loading [*Smith et al.*, 2001], the condensation level rises to altitudes above 40 km. The abundance of water vapor plays a relatively minor role, with the condensation level inversely related to water vapor abundance. This is most clearly seen at places of very low water vapor, such as 40°–50°S latitude from L_s = 60°–210° where the condensation level increases to the south despite warmer temperatures to the north.

The inferred seasonal variation of the water condensation level is large. Water vapor is essentially well mixed throughout the atmosphere for half the year (L_s = 180°–360°), but confined to the lowest scale height or two for the other half of the year (L_s = 0°–180°). This large, seasonal variation in the condensation level is just one more component of the two distinct seasons that appear to exist on present-day Mars, with relatively warm and dusty conditions in the perihelion (southern spring and summer) season, and relatively cool, dust-free, and cloudy conditions in the aphelion (northern spring and summer) season. The seasonal behavior described above for the condensation level was emphasized by *Clancy et al.* [1996] who suggested that the seasonal variation in the height of the water condensation level could play a pivotal role in the transport of water vapor and the observed asymmetry in the latitudinal dependence of

water vapor near solstice. Near perihelion the condensation level is relatively high and water vapor can be transported from south to north via the Hadley circulation without condensing. Near aphelion the condensation level is relatively low and water vapor can not be transported via the Hadley circulation without condensing. This mechanism could explain the relative maximum observed at low northerly latitudes during the fall and winter, and the much larger latitudinal gradient in water vapor in the northern summer as compared to the southern summer.

5.2. Globally-Averaged Trends

The top panel of Fig. 7 shows the total amount of atmospheric water vapor as a function of season integrated over the northern and southern hemispheres and over the entire globe. Condensed water is not included in the total integrated amount of water because its contribution is insignificant. To perform the integration over an entire hemisphere, an estimate was made for water vapor abundance in the high-latitude regions where no results are available because of insufficient thermal contrast between the surface and the atmosphere. In the fall and winter seasons in each hemisphere (L_s = 180°–360° in the northern hemisphere and 0°–180° in the southern hemisphere), a low nominal value of 3 pr-μm water vapor was used to be consistent with the low values retrieved at the highest latitudes where good results were obtained during those seasons (see Plate 1). In the spring and summer seasons, a constant water vapor abundance was extrapolated to the pole from the most poleward retrieved results. These extrapolations have little effect on the hemispherically- and globally-averaged water vapor amounts for two reasons. Firstly, the surface area where water vapor is extrapolated (which is near the pole) is a small fraction of the total surface area over a hemisphere. Secondly, the water vapor values being extrapolated are generally small (except during early summer) and contribute little to the total.

The total global amount of water vapor varies from ~1.0–2.5x10^{15} g (equivalent to 14–35 pr-μm or 1.1–2.7 km^3 ice) during the year. The major seasonal feature in the global amount of water vapor is a ~50% drop from L_s = 310°–360° and a corresponding recovery from L_s = 50°–120°. Both the northern and southern hemispheric totals show maxima in the spring and summer seasons and minima in the fall and winter. The annually-averaged total amount of water vapor is 1.2x10^{15}, 0.7x10^{15}, and 1.9x10^{15} g (equivalent to 17, 9.5, and 13 pr-μm) for the northern hemisphere, southern hemisphere, and the entire globe, respectively.

As expected, the total water vapor amounts shown in Fig. 7 are slightly higher from L_s = 330°–205° than those computed by *Jakosky and Farmer* [1982] and by *Haberle and Jakosky* [1990] using MAWD results, and significantly higher during the dusty L_s = 205°–330° season. Unlike the nearly constant level observed by TES, MAWD results show a significant decrease in the global amount of water vapor between L_s = 170° and 320° because of the two planet-encircling dust storms that occurred during 1977 at that time.

The changes in total atmospheric water vapor as a function of season give clues to the important large-scale sources, sinks, and transport processes for water vapor. Between L_s = 50° and 120°, northern hemisphere water vapor increases dramatically while southern hemisphere water vapor remains at a nearly constant low level. The increase in northern hemisphere water vapor occurs primarily at middle and high latitudes (see Plates 1 and 2) and so the likely sources for the water vapor are the receding seasonal ice cap and the release of water adsorbed into the regolith. The north residual polar cap can also contribute to the increase in northern hemisphere water toward the end of this period after ~L_s = 80° when it is exposed. The relative importance of the seasonal and residual ice caps versus the regolith as a source (or as a sink) can not be determined from this analysis alone.

The northern hemisphere peak in water vapor abundance lasts for only a short time. During the period L_s = 140°–240°, the amount of northern hemisphere water vapor decreases rapidly to a value less than half of its peak value at L_s = 120°. Although global water vapor shows a small (~20%) decline from L_s = 140°–170°, it is essentially constant from L_s = 170°–320° because of an increase in southern hemisphere water vapor which largely offsets the decrease in northern hemisphere water vapor. This suggests that both non-atmospheric sinks and transport contribute to the loss of northern hemisphere water vapor. During the first portion of this period (before L_s = 180°), the loss is dominated by incorporation of water back into the residual and seasonal ice caps and by adsorption of water into the regolith. Later, there also appears to be a net transport of water vapor from the northern to the southern hemisphere that is most active between L_s = 150° and 230°.

The amount of northern hemisphere water vapor

stops declining near L_s = 230°, but the amount of southern hemisphere water vapor continues to increase somewhat until reaching a peak at L_s = 290°. During this period, water vapor equatorward of 40°S latitude slowly decreases while water vapor poleward of 40°S latitude rapidly increases. The latitudes where water vapor increases are clear of seasonal CO_2 frost by this time of the year [*Christensen et al.*, 2001], so the source for this increase seems to be primarily from the release of water adsorbed into the regolith and possibly from transport. Beginning at L_s = 310°, southern hemisphere water vapor declines rapidly without a compensating increase in the northern hemisphere water vapor, such that the northern spring season presents a significant minimum in the annual variation of Mars global atmospheric water. This contrast in global water abundance between the northern and southern spring seasons is a major aspect of the north-south asymmetry in atmospheric water behavior, as described in section 5.3. There appears to be little, if any, transport from the southern hemisphere to the northern hemisphere during the decay of the southern summer water vapor maximum. The decline in southern hemisphere water vapor appears to be dominated by losses to the seasonal cap, water vapor being cold-trapped onto the residual CO_2 polar cap, and adsorption into the regolith.

5.3. Hemispheric Asymmetry

The bottom panel of Fig. 7 shows the total amounts of water vapor in the northern and southern hemispheres as a function of season in terms of ΔL_s after spring equinox so that the behavior of the two hemispheres can be directly compared. There are significant asymmetries. The overall level of water vapor throughout the year is higher in the northern hemisphere. The amount of northern hemisphere water vapor never reaches the very low levels that southern hemisphere water vapor does in the fall because a moderate amount of water vapor (at least 10 pr-μm) is maintained at low northerly latitudes during the entire year (see Plate 1 and further discussion in section 5.4). Both hemispheres exhibit very similarly-timed early-summer maxima in water vapor and then large decreases in water vapor in late summer and early fall. However, the amplitude of the northern hemisphere maximum is larger, and the time-dependence of the increase in water vapor leading up to the summer maxima are very different for the two hemispheres. In the north, the increase begins rather abruptly at about ΔL_s = 40° and the entire increase occurs between ΔL_s = 40°and 120°. In the south, there is a similarly-timed increase in water vapor (ΔL_s = 40°–120°) but it is much smaller. The majority of the increase in southern hemisphere water vapor occurs earlier during the winter and early spring and appears to be caused by transport of water vapor from the northern to the southern hemisphere. Because of these differences, in the early northern summer (L_s = 100°–140°), the northern hemisphere holds ~85% of the total global atmospheric water, while in the early southern summer (L_s = 280°–320°) the southern hemisphere holds only ~60% of the total global atmospheric water.

Significant asymmetry also currently exists in the seasonal and latitudinal distribution of water vapor between the northern and southern hemispheres. This asymmetry is shown in Plate 2. The water vapor abundances shown in Plate 2 are the same as those shown in the top panel of Plate 1 except that the southern hemisphere data have been "flipped" in latitude (so that south pole is at the top and the equator is at the bottom) and shifted by 180° of L_s relative to the northern hemisphere data so that a direct comparison between the two hemispheres can be made. There are several key differences. As mentioned above, the summertime maximum that is apparent at high latitudes in both hemispheres is about twice as strong in terms of maximum water vapor column abundance in the north as it is in the south. A second key difference is the existence of a deep minimum in water vapor covering the entire southern hemisphere during the fall and early winter. No such minimum exists in the northern hemisphere. In fact, there is more water vapor at low northerly latitudes during the fall and winter than there is in the spring. The third and perhaps most striking difference between the two hemispheres is the completely different behavior of the decay of the summertime maximum between mid-summer and mid-fall. In the northern hemisphere, an area of relatively high water vapor extends increasingly equatorward as the season progresses. Near northern fall equinox the water vapor appears to cross the equator and continue southward eventually contributing to the formation of the summertime maximum in water vapor at high southerly latitudes. In stark contrast, the southern hemisphere maximum rather abruptly decays in middle to late summer with no indication at all of an area of relatively high water vapor extending equatorward, and little indication of northward transport of water vapor.

5.4. Latitude and Longitude Dependence of Water Vapor

In all of the above analysis we have always averaged over longitude to view the dependence of water vapor with L_s and latitude. However, retrieved water vapor column abundance values can also be binned in latitude and longitude (averaging over time) to produce time-averaged latitude-longitude maps. The top panel of Plate 3 shows such a map where the time average is taken over the entire annual cycle. Immediately apparent is an inverse correlation with topography. Hellas shows relatively large water vapor columns while Tharsis shows relatively low water vapor. This kind of inverse correlation implies that the water vapor mixing ratio is constant or a relatively weak function of altitude in the lowest scale height or two where most of the mass of the atmosphere lies. Thus the retrieved results are consistent with our algorithm assumption that water vapor is well-mixed up to the condensation level which is typically 1–1.5 scale heights for L_s = 20°–150° and higher for the rest of the year.

The effect of topography can be removed by dividing retrieved water vapor abundance by a quantity proportional to surface pressure. The bottom panel of Plate 3 shows annually-averaged water vapor divided by the quantity ($p_{\rm surf}$/6.1), where $p_{\rm surf}$ is the annually-averaged surface pressure in mbar. Surface pressures are computed using the topographic map produced by the MGS Mars Orbiter Laser Altimeter (MOLA) team [*Smith et al.*, 1999] along with the annual variation of surface pressure [*Hess et al.*, 1980; *Tillman et al.*, 1993]. A map of annually-averaged surface pressure is shown in Fig. 8. We will use the term "scaled water vapor" for the average annual water vapor abundance divided by ($p_{\rm surf}$/6.1). With this correction, the dependence of water vapor with latitude and longitude that is independent of topography is now apparent.

Figure 9 shows the latitudinal dependence of the scaled water vapor obtained by taking a zonal average of the results shown in Plate 3. The hemispheric asymmetry at middle and high latitudes is caused by hemispheric asymmetry in altitude. When the lower northern hemisphere altitudes are taken account of, the northern and southern hemispheres poleward of 45° latitude are nearly identical. This is a markedly different result than that obtained by *Jakosky and Farmer* [1982] using the MAWD data who found a large gradient in annually-averaged water vapor with twice as much water vapor at high northerly latitudes than at high southerly latitudes (even after correcting for the hemispheric topographic difference).

The most obvious feature in the latitude dependence of scaled water vapor (Fig. 9) is a pronounced maximum between 10°S and 40°N with roughly 50% more water vapor in this latitude band than outside it. The annually-averaged water vapor abundance is high in this latitude band because water vapor is maintained year-round at these latitudes (see Plate 1). Water vapor may be maintained at low northerly latitudes during late northern fall and winter by transport from the southern hemisphere via the Hadley circulation. The northern boundary of the band of high water vapor (~40°N latitude) is likely defined by the southernmost extent of the north seasonal polar cap. Equatorward of that latitude the sinks for water vapor are much reduced and water vapor can remain at a moderate level year-round.

The bottom panel of Plate 3 shows that there are large longitude variations in annually-averaged scaled water vapor equatorward of ~50°N and S latitude. The maximum seen in Fig. 9 (and Plate 1) at 10°S–40°N latitude is primarily caused by two large regions of high water vapor abundance from 60°–150°W longitude (Tharsis) and 300°–10°W longitude (Arabia Terra). Although the highlands around Olympus Mons and the Tharsis volcanoes have a high scaled water vapor, the volcanoes themselves do not. Large longitude variations exist outside of the latitude band of high annually-averaged water vapor as well. At 25°S latitude, scaled water vapor varies from its global minimum of 7.5 pr-μm at 35°W longitude (just south of Margaritifer Sinus) to a value twice as high just 90° of longitude to both the east and west.

The top panel of Fig. 10 shows the albedo of Mars derived from TES visible bolometric observations [*Christensen et al.*, 2001]. The low latitude longitude dependence in scaled water vapor shows a strong positive correlation with albedo (high water vapor in high albedo regions). This same correlation with albedo was also noted by *Jakosky and Farmer* [1982] using MAWD results and by *Rosenqvist et al.* [1992] using results from the ISM instrument on the Phobos spacecraft. At low latitudes water vapor is also anti-correlated with surface pressure [*Smith et al.*, 1999] (Fig. 8), and with thermal inertia [*Mellon et al.*, 2000] (bottom panel of Fig. 10). All three of these quantities (albedo, surface pressure, and thermal inertia) have moderate correlations (or anti-correlations) between them and so it is difficult to sort out the cause and effect. Albedo, thermal

inertia, and surface pressure (topography) have direct relations to the average and diurnal variation of surface and subsurface temperatures, the pore space size and grain size of the regolith, and to the circulation patterns of the atmosphere. These can in turn influence the transport of water vapor and its adsorption and desorption into the regolith. It is likely that a combination of albedo, thermal inertia, and topography contribute to the longitude dependence of annually-averaged water vapor. Poleward of 40°N latitude the correlation of scaled water vapor with albedo, and the anti-correlation with thermal inertia and surface pressure, abruptly vanishes, and perhaps even changes sign. In the southern hemisphere, the correlation of scaled water vapor with albedo persists to at least 60°S latitude. Poleward of that there is little longitude dependence in the scaled water vapor.

Scaled water vapor might still be anti-correlated with surface pressure even after the topography has been "removed" because water vapor is not completely well-mixed through the entire atmosphere. Therefore, dividing by ($p_{\rm surf}/6.1$) can actually be a slight overcompensation for topography. Supporting this idea is the fact that the correlation between scaled water vapor and surface pressure is lower in the southern hemisphere than in the northern hemisphere. For example, Hellas and Argyre do not show up at all in the bottom panel of Plate 3 (scaled water vapor) although Hellas is very prominent in the top panel of Plate 3 (unscaled). In the southern spring and summer when southern hemisphere water vapor abundance is high (and the most contribution to the annual average is made), the condensation level is high and water vapor is more nearly well-mixed throughout the atmosphere. In the northern spring and summer when northern hemisphere water vapor is high the condensation level is lower and water vapor is not as completely well-mixed.

6. Summary

We have developed an algorithm to retrieve water vapor column abundance from TES nadir-geometry spectra using rotational lines from 240–360 cm^{-1}. Observations of water vapor by TES during the Mars Global Surveyor mapping mission now cover over one full Martian year and allow an analysis of the dependence of water vapor on latitude, longitude, and season (L_s) in unprecedented detail.

The TES results show a maximum in water vapor abundance at high latitudes during mid-summer in both hemispheres. The southern hemisphere maximum was not observed by Viking MAWD. Results from MAWD taken between $L_s = 205°$ and 330° appear to be greatly affected by two planet-encircling dust storms. Scattering by dust and water ice biases the MAWD water vapors to lower values since the observed radiation does not sample the entire column of water vapor. As stated by *Jakosky and Farmer* [1982], we believe that MAWD water vapor results from this period must be regarded as lower limits. The TES-derived water vapor results are only very minimally affected by dust scattering because scattering is much less important at TES wavelengths (~30 μm) than at the MAWD wavelength (1.38 μm), and no planet-encircling dust storm was observed during the TES year (1999–2000). Outside of the dusty $L_s = 205°$–330°season, TES and MAWD are generally comparable, although TES results are systematically 10–50% higher than MAWD results, and significant differences are apparent in the details of the dependence on L_s and latitude.

There are large differences in the hemispheric (north versus south) and seasonal (perihelion versus aphelion) behavior of water vapor. The summertime peak in water vapor abundance is roughly twice as high in the north as in the south. The decay of the northern hemispheres summertime maximum leads to a relative maximum in water vapor that extends further southward with time, eventually crossing the equator to the southern hemisphere. The decay of the southern hemisphere summertime maximum has no corresponding northward transport. Water vapor abundance declines monotonically at all latitudes at the end of southern summer.

Primarily because of the seasonal dependence of atmospheric temperatures, there is a strong seasonal dependence on the water condensation level. The condensation level is typically 10–15 km (1–1.5 scale heights) above the surface during the aphelion season ($L_s = 0°$–180°), but greater than 30 km (¿3 scale heights) during the perihelion season ($L_s = 180°$–360°). This means that water vapor is confined to lower altitudes in the aphelion season, and transport between the two hemispheres seems to be influenced by this. A very steep latitudinal gradient in water vapor abundance forms during the aphelion season (high in the north), while water vapor is spread more uniformly in latitude during the perihelion season.

The annually-averaged amount of water vapor is 17 pr-μm in the northern hemisphere and 9.5 pr-μm in the southern hemisphere. However, when the ef-

fect of topography is removed, the annually-averaged amount of water vapor becomes 17 pr-μm (referenced to a 6.1 mbar pressure surface) in the latitude band from 10°S–40°N, and 12 pr-μm everywhere else. Northerly and southerly high latitudes have the same scaled water vapor abundance. This latitudinal dependence is very different than the analysis of MAWD results by *Jakosky and Farmer* [1982] which showed a large gradient from north to south in annually-averaged water vapor abundance even after correction for topography. The latitude and longitude dependence of annually-averaged water vapor retrieved by TES (corrected for topography) has a significant positive correlation with albedo and significant negative correlations with thermal inertia and surface pressure.

Additional analysis and observations promise to make the TES data set an even more useful and comprehensive tool for the study of the Martian water cycle. Continued observations by TES during the Mars Global Surveyor extended mission will provide the amount of interannual variability between two consecutive Martian years, and further analysis of the existing TES spectra taken in the limb-geometry will provide crucial information about the vertical structure and diurnal (~0200 versus ~1400 local time) dependence of water vapor.

Acknowledgments. We thank Todd Clancy, John Pearl, and Barney Conrath for numerous suggestions and for providing detailed early reviews of this paper. We thank Bruce Jakosky for providing the Viking MAWD results in tabular form, and Terry Martin for providing the Viking IRTM dust opacity results in digital form. We thank Monte Kaelberer and Ever Guandique for providing software development and data-handling expertise at Goddard Space Flight Center, and Bill Maguire for advice on spectroscopic issues. We thank Mike Wolff for help with constructing the line-by-line code used to compute synthetic water vapor transmittances. We also thank the TES operations team at Arizona State University, including Kelly Bender, Noel Gorelick, Greg Mehall, and Kim Murray, and the entire spacecraft and mission operations teams at the Jet Propulsion Lab and Lockheed Martin. Finally, we thank Phil Christensen, PI of the TES instrument, for all the work he has done to provide this spectacular data set.

References

Bandfield, J. L., V. E. Hamilton, and P. R. Christensen, A global view of Martian surface composition from MGS-TES, *Science, 287*, 1626–1630, 2000.

Bandfield, J. L., P. R. Christensen, and M. D. Smith, Spectral data set factor analysis and end-member recovery: Application to analysis of Martian atmospheric particulates, *J. Geophys. Res., 105*, 9573–9588, 2000.

Barker, E. S., R. A. Schorn, A. Woszczyk, R. G. Tull, and S. J. Little, Mars: Detection of atmospheric water vapor during the southern hemisphere spring and summer seasons, *Science, 170*, 1308–1310, 1970.

Burgdorf, M. J., et al., ISO observations of Mars: An estimate of the water vapor vertical distribution and the surface emissivity, *Icarus, 145*, 79–90, 2000.

Christensen, P. R., Calibration report for the Thermal Emission Spectrometer (TES) for the Mars Global Surveyor Mission, Mars Global Surveyor Project, Jet Propul. Lab., Pasadena, Calif., 1999.

Christensen, P. R., et al., Thermal Emission Spectrometer Experiment: Mars Observer Mission, *J. Geophys. Res., 97*, 7719–7734, 1992.

Christensen, P. R., et al., Results from the Mars Global Surveyor Thermal Emission Spectrometer, *Science, 279*, 1692–1698, 1998.

Christensen, P. R., et al., Detection of crystalline hematite mineralization on Mars by the Thermal Emission Spectrometer: Evidence for near-surface water, *J. Geophys. Res., 105*, 9623–9642, 2000.

Christensen, P. R., et al., The Mars Global Surveyor Thermal Emission Spectrometer Experiment: Investigation description and surface science results, *J. Geophys. Res.*, in press, 2001.

Clancy, R. T., A. W. Grossman, and D. O. Muhleman, Mapping Mars Water Vapor with the Very Large Array, *Icarus, 100*, 48–59, 1992.

Clancy, R. T., A. W. Grossman, M. J. Wolff, P. B. James, Y. N. Billawalla, B. J. Sandor, S. W. Lee, and D. J. Rudy, Water vapor saturation at low altitudes around Mars aphelion: A key to Mars climate?, *Icarus, 122*, 36–62, 1996.

Colburn, D. S., J. B. Pollack, and R. M. Haberle, Diurnal variations in optical depth at Mars, *Icarus, 79*, 159–189, 1989.

Conrath, B. J., J. C. Pearl, M. D. Smith, W. C. Maguire, S. Dason, M. S. Kaelberer, and P. R. Christensen, Mars Global Surveyor Thermal Emission Spectrometer (TES) observations: Atmospheric temperatures during aerobraking and science phasing, *J. Geophys. Res., 105*, 9509–9520, 2000.

Crisp, D., D. A. Allen, D. H. Grinspoon, and J. B. Pollack, The dark side of Venus: Near-infrared images and spectra from the Anglo-Australian Observatory, *Science, 253*, 1263–1266, 1991.

Davies, D. W., The vertical distribution of Mars water vapor, *J. Geophys. Res., 84*, 2875–2880, 1979.

Farmer, C. B., D. W. Davies, A. L. Holland, D. P. La Porte, and P. E. Doms, Mars: Water vapor observations from the Viking orbiters, *J. Geophys. Res., 82*, 4225–4248, 1977.

Gamache, R. R., S. P. Neshyba, J. J. Plateaux, A. Barbe, L. Régalia, and J. B. Pollack, CO_2-broadening of water-vapor lines, *J. Molec. Spect., 170*, 131–151, 1995.

Goody, R., R. West, L. Chen, and D. Crisp, The correlated-k method for radiation calculations in nonhomogeneous atmospheres, *J. Quant. Spect. Rad. Trans., 42*, 539–550, 1989.

Gurwell, M. A., et al., Submillimeter Wave Astronomy Satellite observations of the Martian atmosphere: Temperature and vertical distribution of water vapor, *ApJ, 539*, L143–L146, 2000.

Haberle, R. M., and B. M. Jakosky, Sublimation and transport of water from the north residual polar cap on Mars, *J. Geophys. Res., 95*, 1423–1437, 1990.

Hanel, R. A., et al., Investigation of the Martian environment by infrared spectroscopy on Mariner 9, *Icarus, 17*, 423–442, 1972.

Hess, S. L., J. A. Ryan, J. E. Tillman, R. M. Henry, and C. B. Leovy, The annual cycle of pressure on Mars measured by Viking Landers 1 and 2. *Geophys. Res. Lett., 7*, 197–200, 1980.

Hinson, D. P., R. A. Simpson, J. D. Twicken, G. L. Tyler, and F. M. Flasar, Initial results from radio occultation measurements with Mars Global Surveyor, *J. Geophys. Res., 104*, 26,997–27,012, 1999.

Howard, T. N., D. E. Burch, and D. Williams, Infrared transmission of synthetic atmospheres, *J. Opt. Soc. Am., 46*, 186–190, 237–245, 334–338, 452–455, 1956.

Husson, N., B. Bonnet, N. A. Scott, and A. Chedin, Management and study of spectroscopic information – The GEISA program, *J. Quant. Spec. Rad. Transf., 48*, 509–518, 1992.

Jakosky, B. M., The seasonal cycle of water on Mars, *Space Sci. Rev., 41*, 131–200, 1985.

Jakosky, B. M., and C. B. Farmer, The Seasonal and Global Behavior of Water Vapor in the Mars Atmosphere: Complete Global Results of the Viking Atmospheric Water Detector Experiment, *J. Geophys. Res.*, it 87, 2999–3019, 1982.

Jakosky, B. M., and E. S. Barker, Comparison of ground-based and Viking Orbiter measurements of Martian water vapor: Variability of the seasonal cycle, *Icarus, 57*, 322–334, 1984.

Jakosky, B. M., and R. M. Haberle, The Seasonal behavior of water on Mars, in *Mars*, edited by H. H. Kieffer et al., pp. 969–1016, Univ. of Ariz. Press, Tucson, 1992.

Liebe, H. J., and T. A. Dillon, Accurate foreign-gas-broadening parameters of the 22-GHz H_2O line from refraction spectroscopy, *J. Chem. Phys., 50*, 727–732, 1969.

Martin, T. Z., Thermal infrared opacity of the Martian atmosphere, *Icarus, 66*, 2–21, 1986.

Martin, T. Z., and M. I. Richardson, New dust opacity mapping from Viking infrared thermal mapper data, *J. Geophys. Res., 98*, 10,941–10,949, 1993.

Mellon, M. T., B. M. Jakosky, H. H. Kieffer, and P. R. Christensen, High-resolution thermal inertia mapping from the Mars Global Surveyor Thermal Emission Spectrometer, *Icarus, 148*, 437–455, 2000.

Novak, R., M. Mumma, M. DiSanti, N. Dello Russo, and K. Magee-Sauer, Photochemical mapping of ozone and water in the atmosphere of Mars near the 1997 aphelion, Submitted to *Icarus*, 2001.

Pearl, J. C., B. J. Conrath, M. D. Smith, J. L. Bandfield, and P. R. Christensen, Mars water-ice clouds: Observations by the Thermal Emission Spectrometer (TES) during the first martian year, *J. Geophys. Res.*, (in press), 2001.

Pollack, J. B., D. S. Colburn, R. Kahn, J. Hunter, W. Van Camp, C. E. Carlston, and M. R. Wolf, Properties of aerosols in the Martian atmosphere, as inferred from Viking lander imaging data, *J. Geophys. Res., 82*, 4479–4496, 1977.

Pollack, J. B., et al., Near-infrared light from Venus' nightside: A spectroscopic analysis, *Icarus, 103*, 1–42, 1993.

Rizk, B., W. K. Wells, and D. M. Hunten, Meridional Martian water abundance profiles during the 1988–1989 season, *Icarus, 90*, 205–213, 1991.

Rodin, A. V., O. I. Korablev, and V. I. Moroz, Vertical distribution of water in the near-equatorial troposphere of Mars: water vapor and clouds, *Icarus, 125*, 212–229, 1997.

Rosenqvist, J., P. Drossart, M. Combes, T. Encrenaz, E. Lellouch, J. P. Bibring, S. Erard, Y. Langevin, and E. Chassefière, Minor constituents in the Martian atmosphere from the ISM/Phobos experiment, *Icarus, 98*, 254–270, 1992.

Smith, D. E., et al., The global topography of Mars and implications for surface evolution, *Science, 284*, 1495–1503. 1999.

Smith, M. D., J. C. Pearl, B. J. Conrath, and P. R. Christensen, Mars Global Surveyor Thermal Emission Spectrometer (TES) observations of dust opacity during aerobraking and science phasing, *J. Geophys. Res., 105*, 9539–9552, 2000a.

Smith, M. D., J. L. Bandfield, and P. R. Christensen, Separation of atmospheric and surface spectral features in Mars Global Surveyor Thermal Emission Spectrometer (TES) spectra, *J. Geophys. Res., 105*, 9589–9608, 2000b.

Smith, M. D., J. C. Pearl, B. J. Conrath, and P. R. Christensen, Recent TES results: Mars water vapor abundance and the vertical distribution of aerosols, *Bull. Amer. Astron. Soc., 32*, 1094, 2000c.

Smith, M. D., J. C. Pearl, B. J. Conrath, and P. R. Christensen, Thermal Emission Spectrometer results: Mars atmospheric thermal structure and aerosol distribution,

J. Geophys. Res., in press, 2001.

Smith, P. H., et al., Results from the Mars Pathfinder Camera, *Science*, *278*, 1758–1765, 1997.

Spinrad, H., G. Münch, L. D. Kaplan, The detection of water vapor on Mars, *ApJ*, 137, 1319–1321, 1963.

Sprague, A. L., D. M. Hunten, and R. E. Hill, Martian water vapor, 1988–1995, *J. Geophys. Res.*, *101*, 23229–23241, 1996.

Sprague, A. L., D. M. Hunten, R. E. Hill, L. R. Doose, and B. Rizk, Water vapor abundances over Mars north high latitude regions: 1994–1996, *Icarus*, in press, 2001.

Tillman, J. E., N. C. Johnson, P. Guttorp, and D. B. Percival, The Martian annual atmospheric pressure cycle – Years without great dust storms, *J. Geophys. Res.*, *98*, 10,963–10,971, 1993.

Titov, D. V., M. J. Markiewicz, N. Thomas, H. U. Keller, R. M. Sablotny, M. G. Tomasko, M. T. Lemmon, and P. H. Smith, Measurements of the atmospheric water vapor on Mars by the Imager for Mars Pathfinder, *J. Geophys. Res.*, *104*, 9019–9026, 1999.

M. D. Smith, NASA Goddard Space Flight Center, Code 693, Greenbelt, MD 20771. (Michael.D.Smith.1@gsfc.nasa.gov)

Received May 31, 2001; revised November xxx, 2001; accepted xxx xxx, 2001.

This preprint was prepared with AGU's LaTeX macros v5.01. File TES˙WaterVapor formatted October 30, 2001.

Figure 1. A synthetic line-by-line spectrum of water vapor convolved to the TES resolution of 6.25 cm^{-1} for the wavelengths used in this analysis for typical conditions (solid line). The spectrum is shown in terms of opacity. The filled boxes show the best-fit wavenumber locations for the TES samples in the 6.25 cm^{-1} resolution mode. The numbers refer to TES sample numbers. The five water vapor band peaks used in this analysis (centered near TES samples 20, 26, 30, 35, and 40) are separated by roughly 5 TES samples or 25 cm^{-1}.

Figure 2. A comparison of averaged TES spectra at 6.25 cm^{-1} (solid line, filled boxes) and 12.5 cm^{-1} (dotted line, open boxes) spectral resolution taken at the same season and latitude (L_s = 306°–308°and 78°–80°S latitude). Spectra are shown in terms of opacity. Water vapor bands are much better defined at 6.25 cm^{-1}.

Figure 3. The relationship between water vapor band depth computed using TES data taken in the 12.5 cm^{-1} resolution mode ($\tau_{12.5}$) and that taken in the 6.25 cm^{-1} resolution mode ($\tau_{6.25}$). A nearly linear relation exists allowing band depth at 12.5 cm^{-1} resolution to be converted to an equivalent band depth at 6.25 cm^{-1} resolution. The linear fit is given by $\tau_{6.25} = 1.45\ (\tau_{12.5} - 0.0035)$.

Figure 4. An example of the fit between the observed averaged TES spectrum (open boxes and solid line) and the best-fit synthetic spectrum (stars and dotted line) for one particular L_s/latitude bin (centered at 43°N latitude, L_s = 85°) shown in terms of opacity. An opacity continuum has been removed from the observed spectrum. A water vapor column abundance of 25 pr-μm is indicated.

Figure 5. Contour map of the ratio of water vapor abundance derived from TES spectra to the water vapor abundance derived from MAWD data [*Jakosky and Farmer*, 1982] as a function of L_s and latitude. The shading represents L_s and latitudes where Viking IRTM measurements showed 9-μm dust opacity >0.4 [*Martin and Richardson*, 1993]. The solid lines bounding the contours on the top and bottom represent the latitude extent of where both TES and MAWD results exist. Planet-encircling dust storms occurred at L_s = 205° and 270°. The times and locations of high dust opacity (shaded areas) correspond to the times and locations of high TES/MAWD water vapor ratio.

Figure 6. The height in km above the surface of the water condensation level as a function of L_s and latitude. Contour levels higher than 40 km above the surface are not shown. The solid lines bounding the contours on the top and bottom represent the latitude extent of where results exist.

Figure 7. The top panel shows total amount of atmospheric water vapor as a function of season for the northern hemisphere (dashed line), the southern hemisphere (dotted line), and the entire globe (solid line). The bottom panel shows the hemispheric data in the top panel replotted to allow direct seasonal comparison of the two hemispheres. Season is expressed as ΔL_s from spring equinox (L_s = 0° for the northern hemisphere and L_s = 180° for the southern hemisphere). Equivalent values are 1 km^3 of ice is 0.917x10^{15} g, and 10 pr-μm over a hemisphere is 0.723x10^{15} g.

Figure 8. Map of the annual average value of surface pressure in mbar based on MOLA data [*Smith et al.*, 1999]. In this map, quantities have been smoothed by the same amount as the contours shown in Plate 3.

Figure 9. The latitudinal behavior of the annually-averaged water vapor abundance, and the latitudinal behavior of the annually-averaged water vapor abundance divided by (p_{surf}/6.1) to remove the effect of topography.

Figure 10. Maps of (top) broadband visual albedo, and (bottom) thermal inertia in J/m^2 K $s^{1/2}$. In these maps, quantities have been smoothed by the same amount as the contours shown in Plate 3. The albedo [*Christensen et al.*, 2001] and the thermal inertia [*Mellon et al.*, 2001] maps are from TES measurements.

Plate 1. The column abundance of water vapor as a function of L_s and latitude: (top) as observed by TES. Contours show a smoothed representation of the results, and (bottom) as observed by Viking MAWD [*Jakosky and Farmer*, 1982].

Plate 2. The distribution of water vapor as a function of season and latitude for the (top) northern and (bottom) southern hemispheres. Season is expressed as ΔL_s from spring equinox ($L_s = 0°$ for the northern hemisphere and $L_s = 180°$ for the southern hemisphere). Both hemispheres are shown with the pole at the top and the equator at the bottom for direct comparison. Contours show a smoothed representation of the results.

Plate 3. Maps of (top) seasonally-averaged water vapor column abundance and (bottom) seasonally-averaged water vapor column abundance divided by ($p_{\rm surf}/6.1$) to remove the effect of topography. Contours show a smoothed representation of the maps.

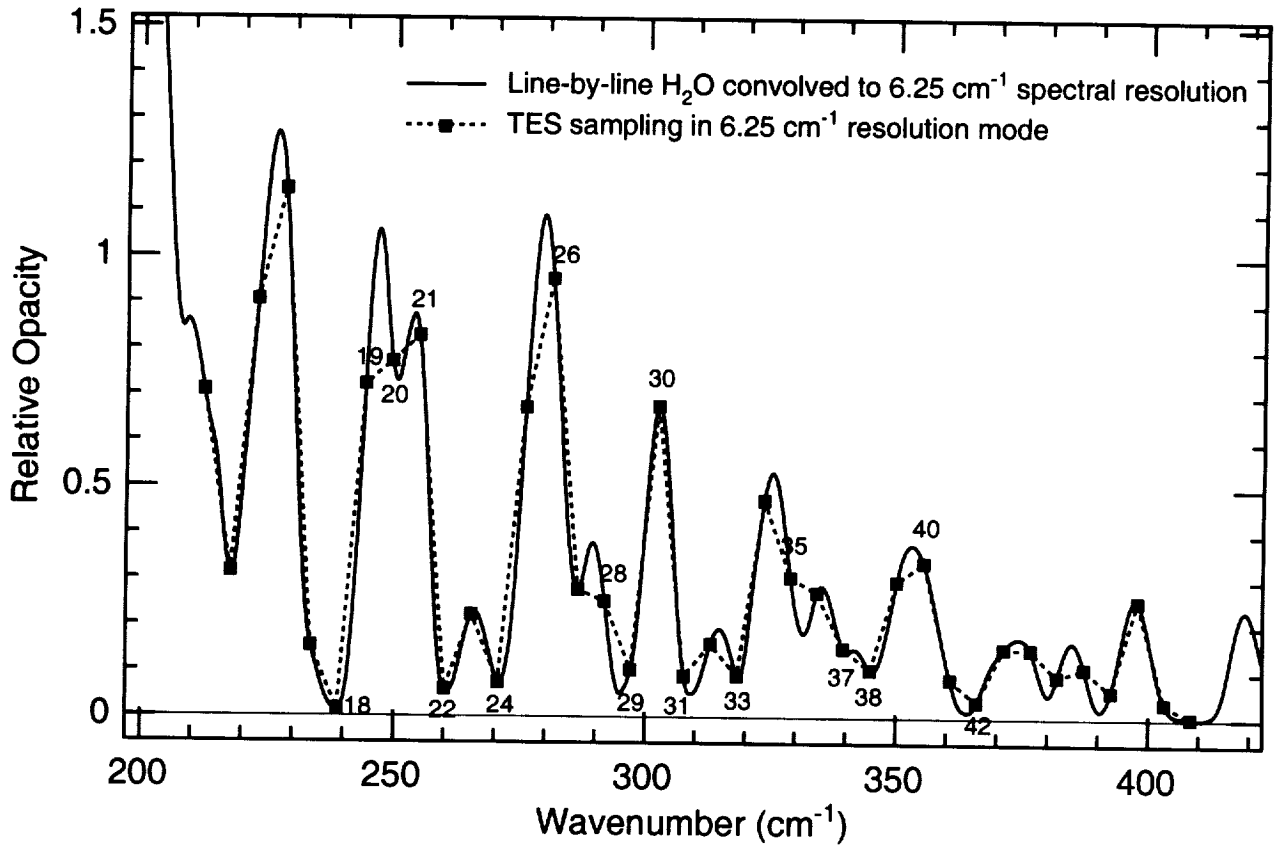
Line-by-line H_2O convolved to 6.25 cm^{-1} spectral resolution
TES sampling in 6.25 cm^{-1} resolution mode
Relative Opacity
Wavenumber (cm^{-1})
1.5
1
0.5
0
200
250
300
350
400
18
19
20
21
22
24
26
28
29
30
31
33
35
37
38
40
42

Fig. 1

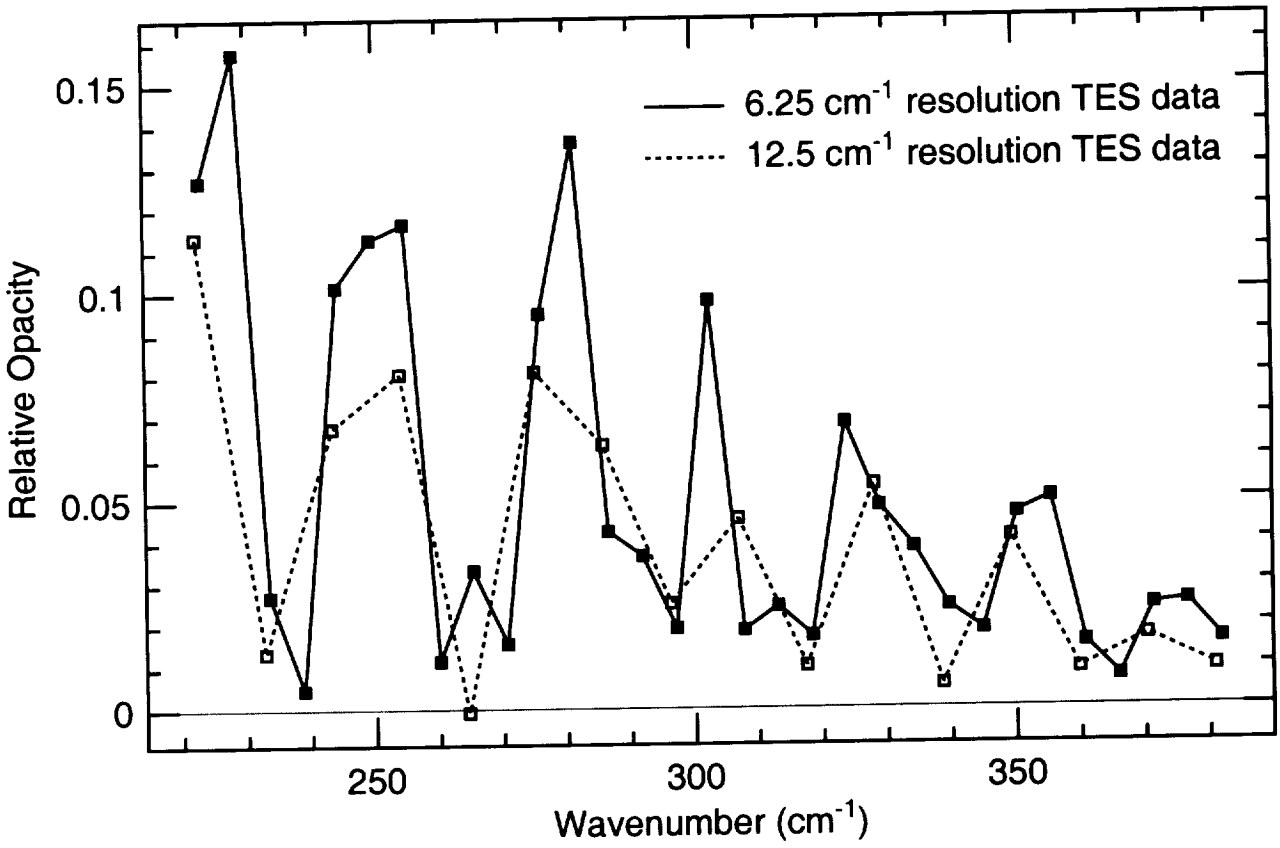
0.15
0.1
0.05
0
Relative Opacity
250
300
350
Wavenumber (cm-1)
6.25 cm-1 resolution TES data
12.5 cm-1 resolution TES data

Fig. 2

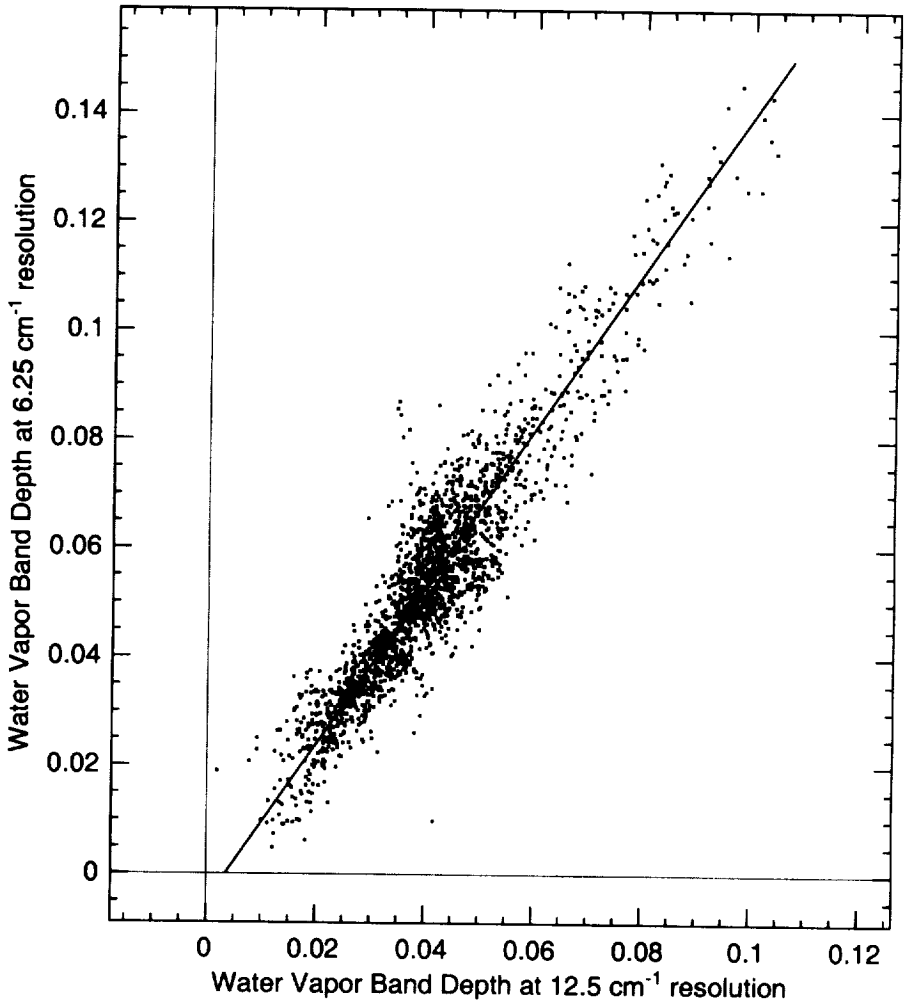
0.14
0.12
0.1
0.08
0.06
0.04
0.02
0
Water Vapor Band Depth at 6.25 cm-1 resolution
0
0.02
0.04
0.06
0.08
0.1
0.12
Water Vapor Band Depth at 12.5 cm-1 resolution

Fig. 3

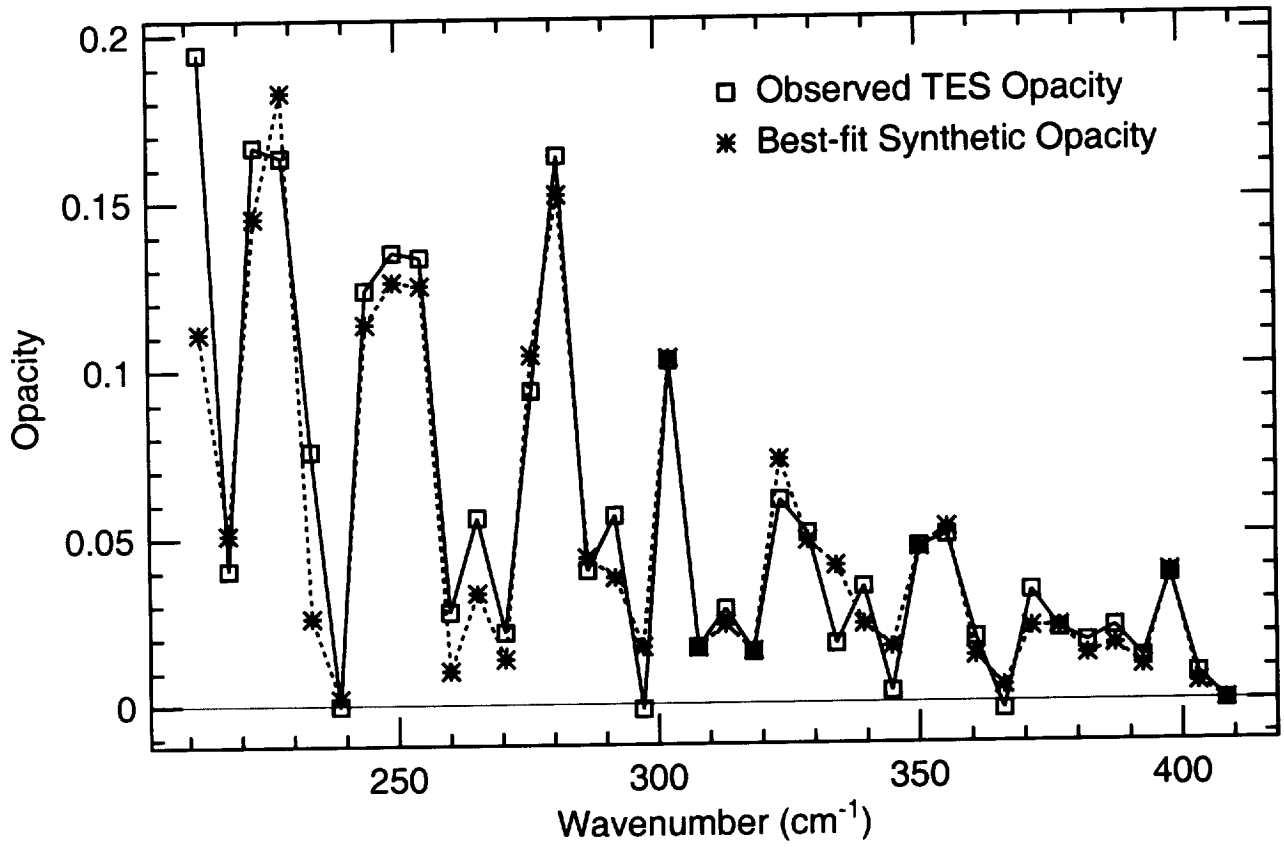
0.2
0.15
0.1
0.05
0
Opacity
250
300
350
400
Wavenumber (cm-1)
Observed TES Opacity
Best-fit Synthetic Opacity

Fig. 4

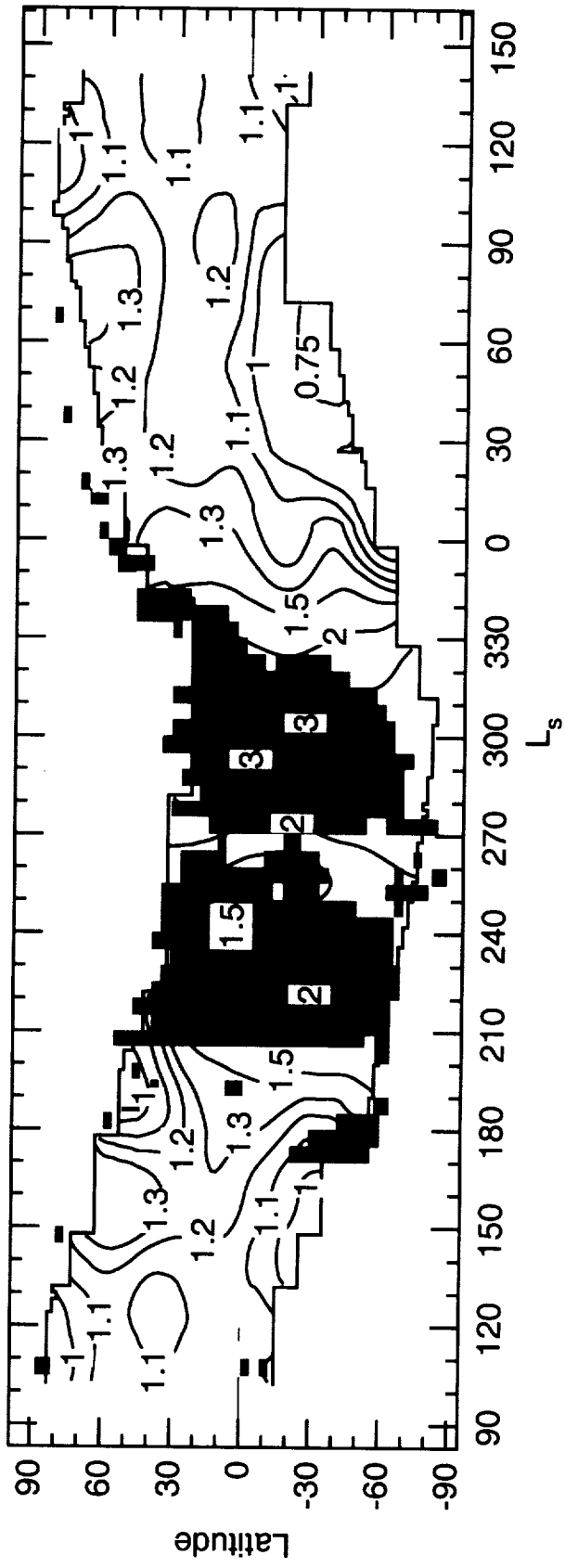
Latitude
90
60
30
0
-30
-60
-90
L_s
0
30
60
90
120
150
180
210
240
270
300
330
0
30
60
90
120
150
0.75
1
1.1
1.2
1.3
1.5
2
3

Fig. 5

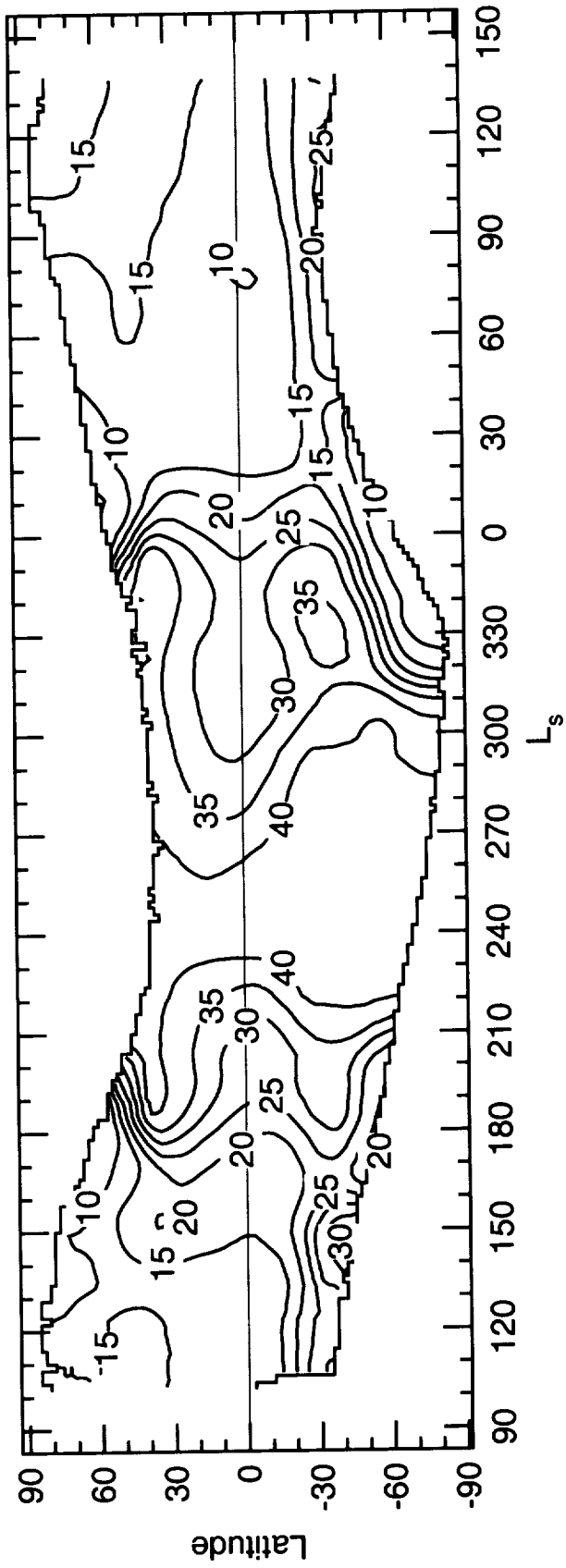
Latitude
90
60
30
0
-30
-60
-90
L_s
0
30
60
90
120
150
180
210
240
270
300
330
10
15
20
25
30
35
40

Fig. 6

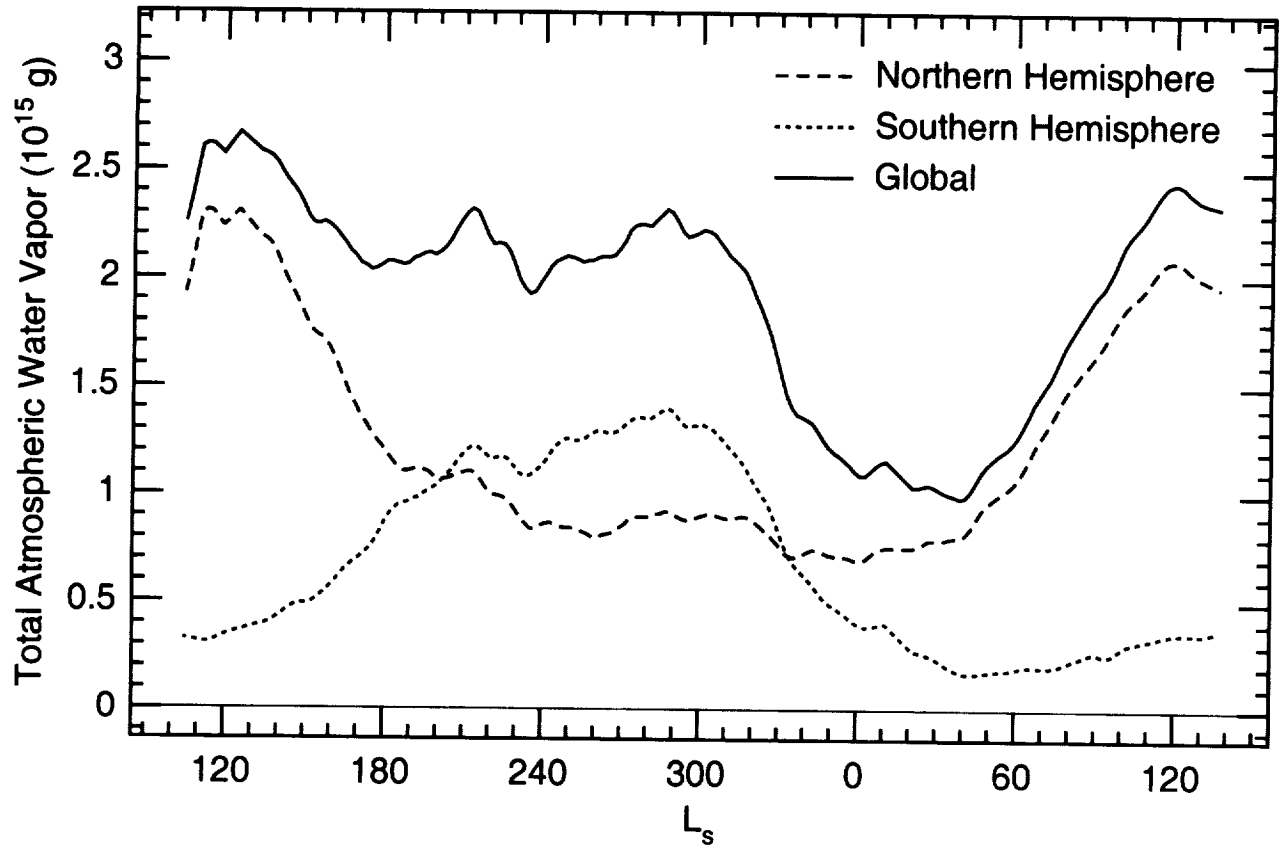
Northern Hemisphere
Southern Hemisphere
Global
Total Atmospheric Water Vapor (10^{15} g)
3
2.5
2
1.5
1
0.5
0
120
180
240
300
0
60
120
L_s

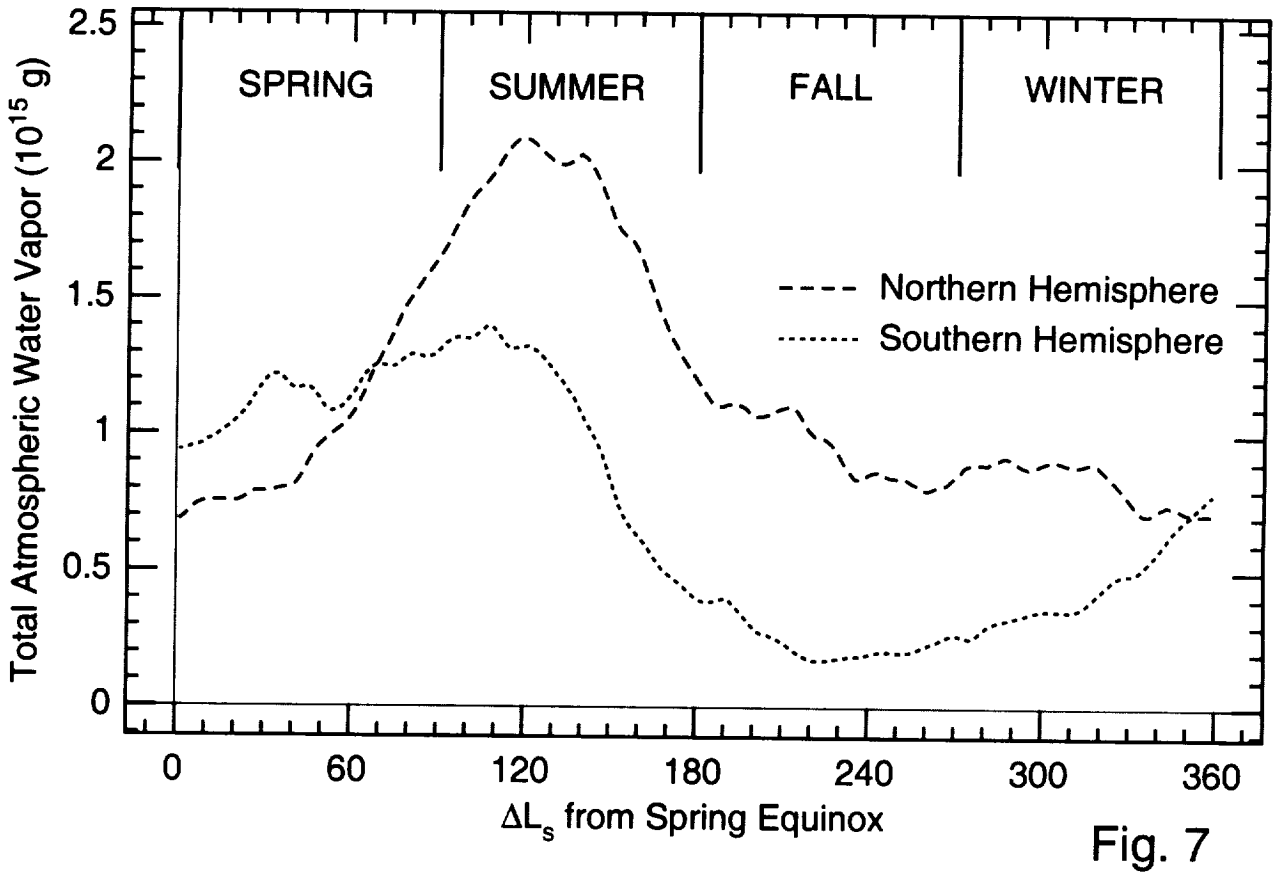
SPRING
SUMMER
FALL
WINTER
Northern Hemisphere
Southern Hemisphere
Total Atmospheric Water Vapor (10^{15} g)
2.5
2
1.5
1
0.5
0
0
60
120
180
240
300
360
ΔL_s from Spring Equinox

Fig. 7

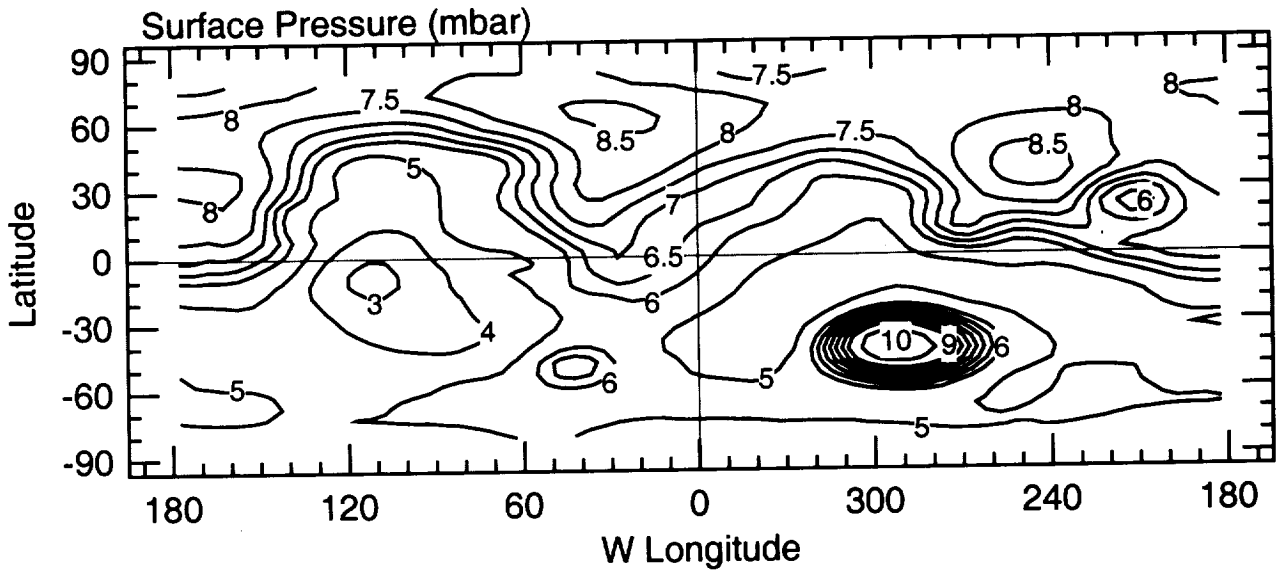
Surface Pressure (mbar)
90
60
30
0
-30
-60
-90
Latitude
180
120
60
0
300
240
180
W Longitude
7.5
8
8.5
7
6.5
6
5
4
3
10
9

Fig. 8

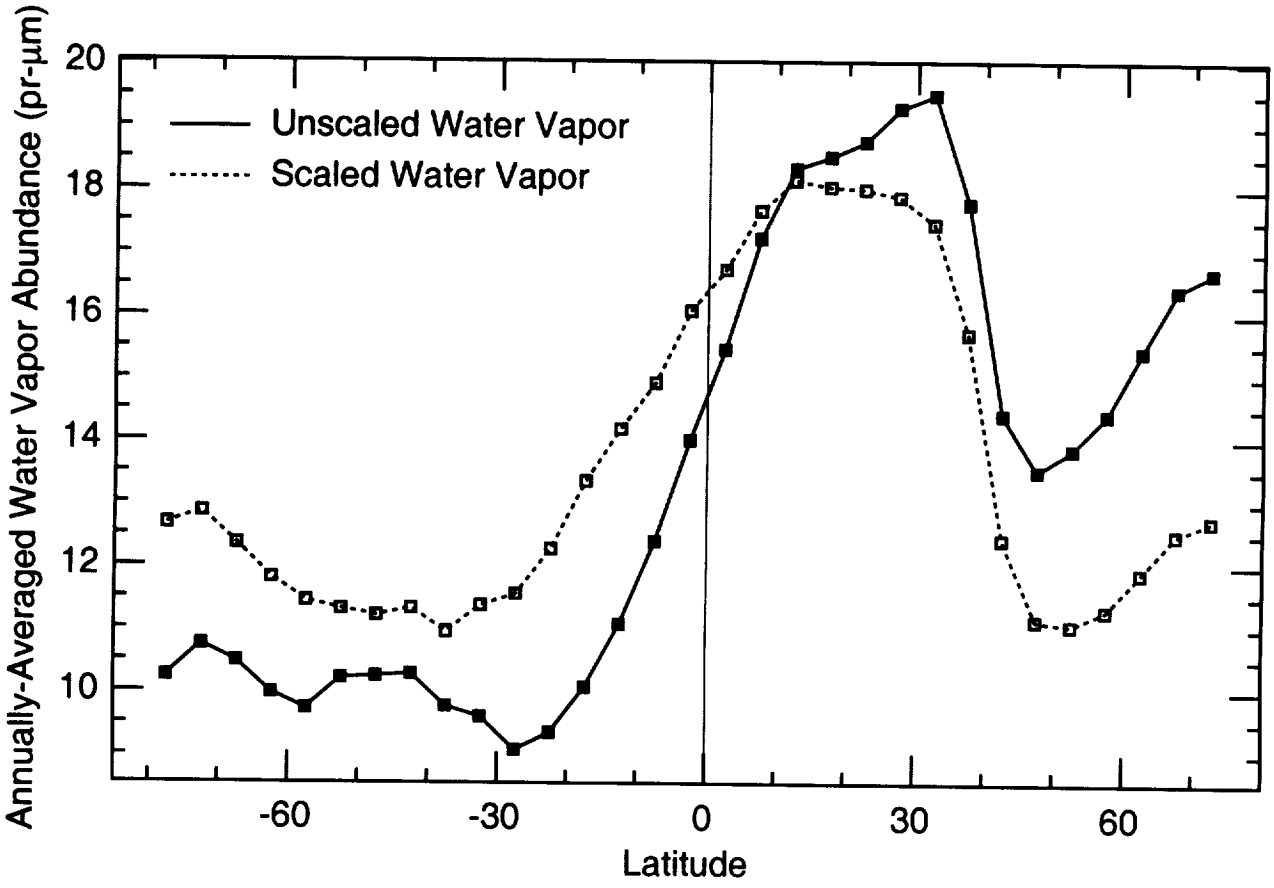
Annually-Averaged Water Vapor Abundance (pr-μm)
20
18
16
14
12
10
Unscaled Water Vapor
Scaled Water Vapor
-60
-30
0
30
60
Latitude

Fig. 9

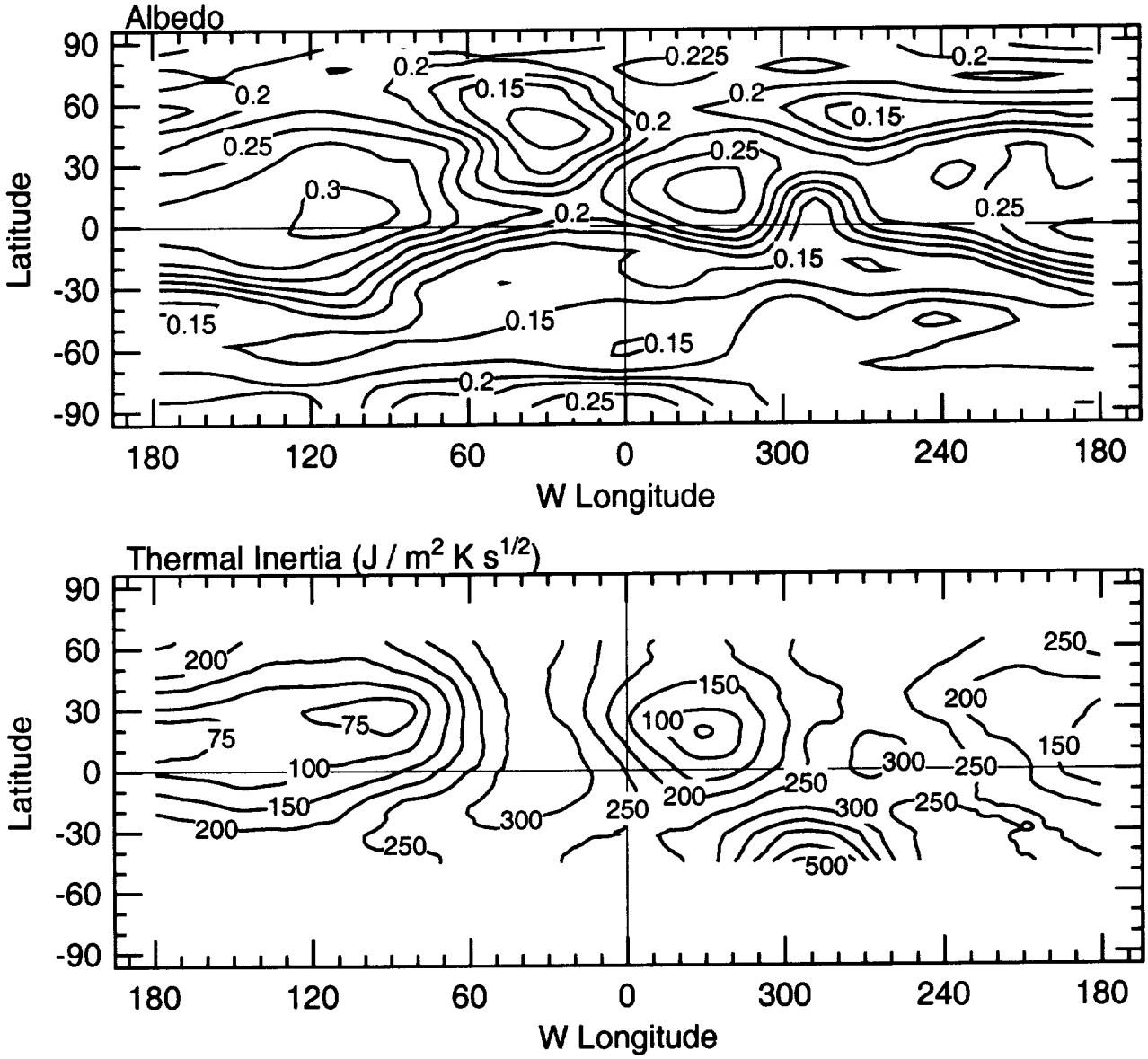
Albedo
90
60
30
0
-30
-60
-90
Latitude
0.2
0.225
0.15
0.25
0.3
180
120
60
0
300
240
180
W Longitude
Thermal Inertia (J / m^2 K s$^{1/2}$)
200
75
100
150
250
300
500
W Longitude

Fig. 10

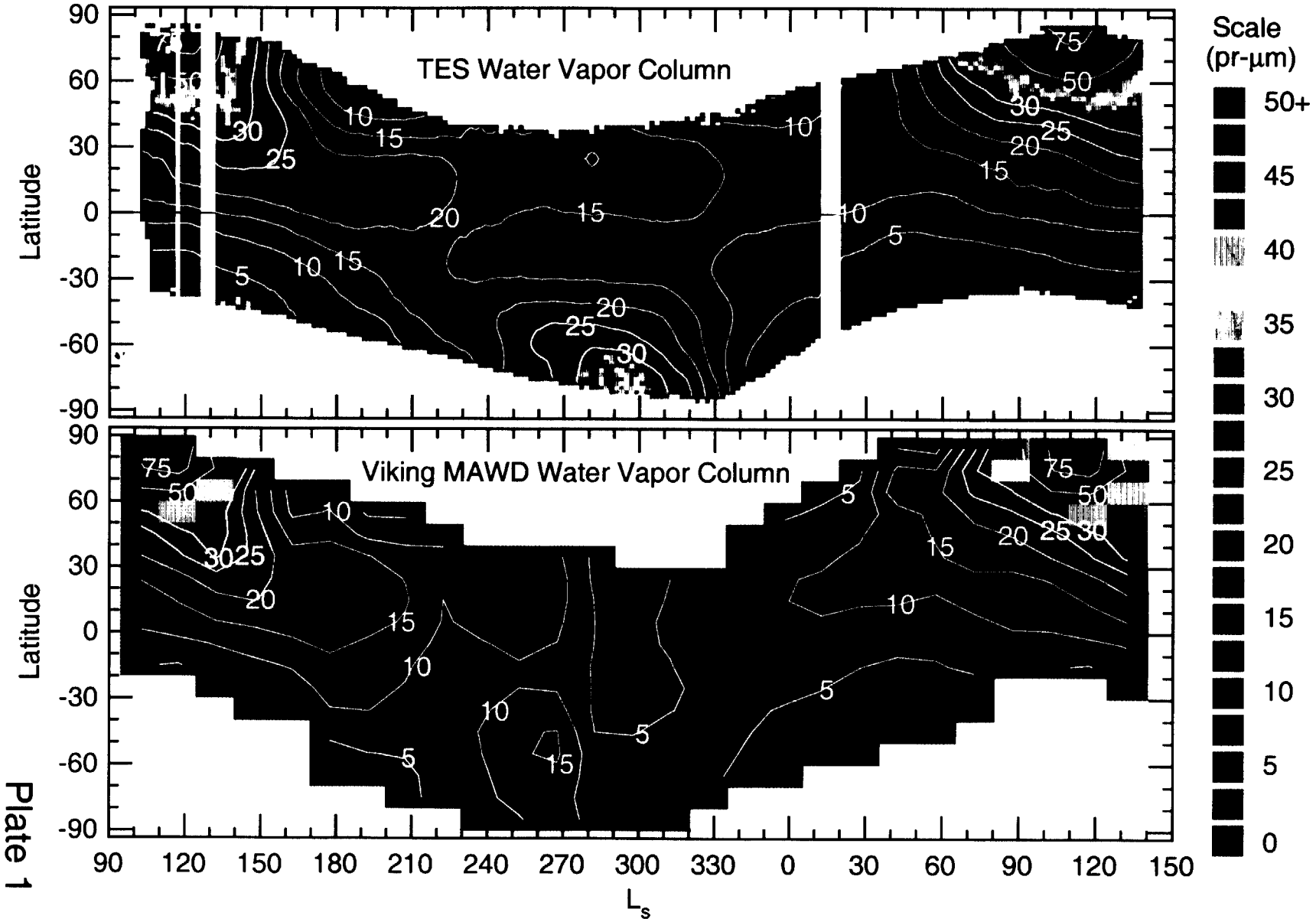
TES Water Vapor Column
Viking MAWD Water Vapor Column
Latitude
Latitude
90
60
30
0
-30
-60
-90
90 120 150 180 210 240 270 300 330 0 30 60 90 120 150
L_s
Scale (pr-μm)
50+
45
40
35
30
25
20
15
10
5
0

Plate 1

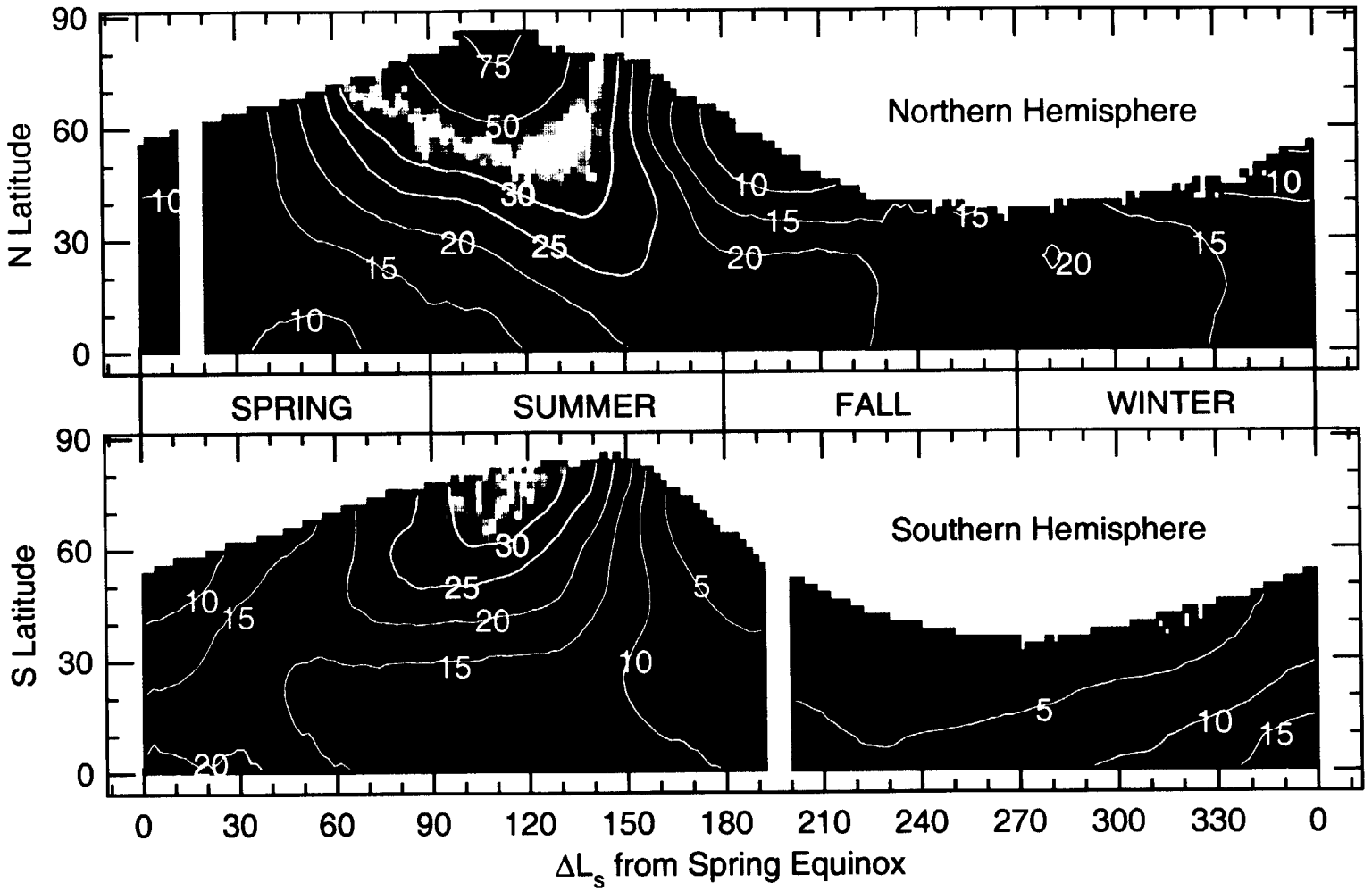
Northern Hemisphere
Southern Hemisphere
N Latitude
S Latitude
SPRING
SUMMER
FALL
WINTER
90
60
30
0
75
50
30
25
20
15
10
5
0 30 60 90 120 150 180 210 240 270 300 330 0
ΔL$_s$ from Spring Equinox

Plate 2

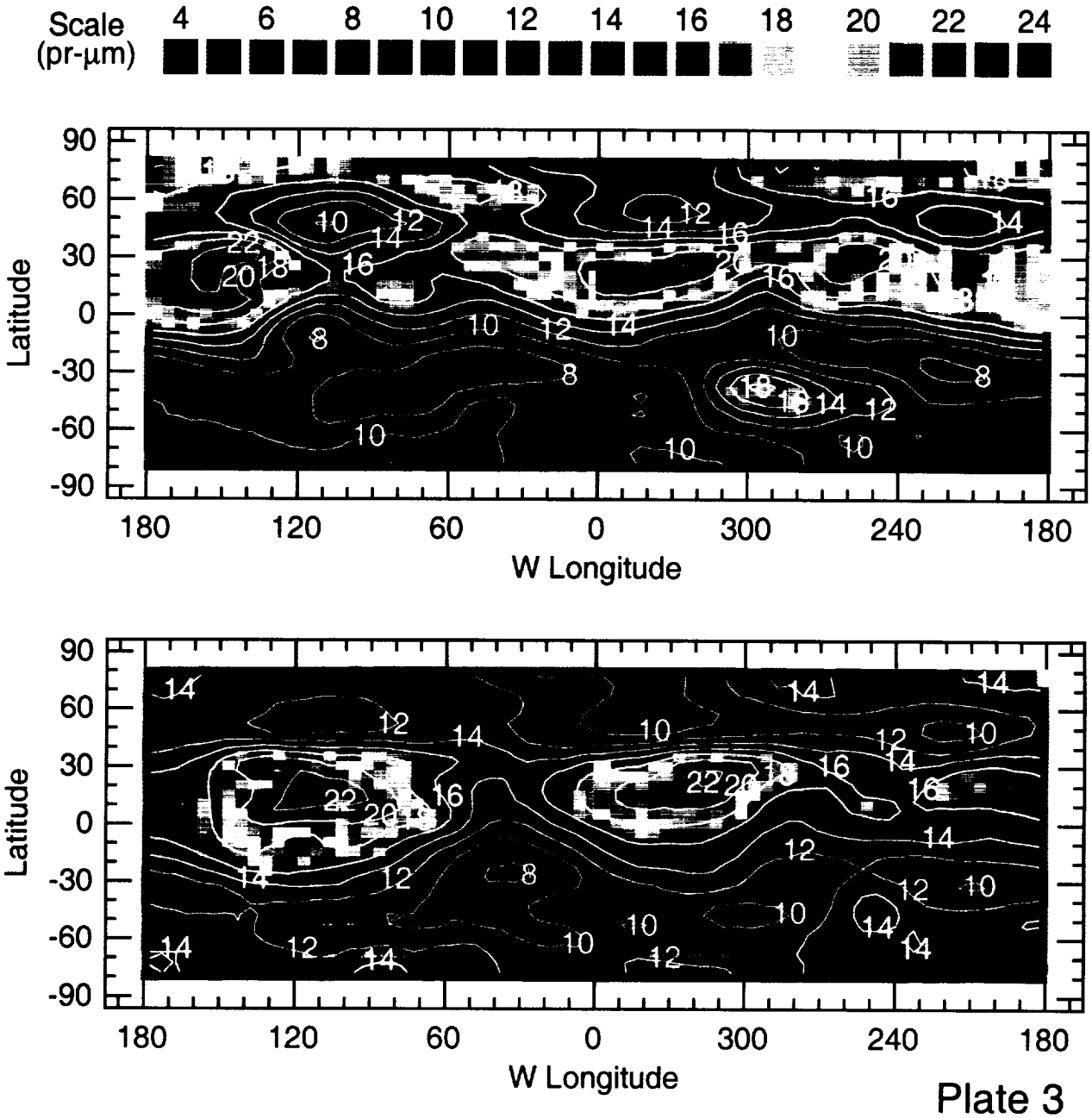
Scale
(pr-μm)
4 6 8 10 12 14 16 18 20 22 24
Latitude
90 60 30 0 -30 -60 -90
180 120 60 0 300 240 180
W Longitude
Latitude
90 60 30 0 -30 -60 -90
180 120 60 0 300 240 180
W Longitude

Plate 3